
IMPROVING FINE-GRAINED CONTROL VIA AGGREGATION OF MULTIPLE DIFFUSION MODELS

Conghan Yue, Zhengwei Peng, Shiyan Du

Sun Yat-Sen University

Zhi Ji

University of Toronto

Chuangjian Cai, Le Wan

Game AI Center, Tencent

Dongyu Zhang *

Sun Yat-Sen University

ABSTRACT

While many diffusion models perform well when controlling particular aspects such as style, character, and interaction, they struggle with fine-grained control due to dataset limitations and intricate model architecture design. This paper introduces a novel training-free algorithm, independent of denoising network architectures, for fine-grained generation, called Aggregation of Multiple Diffusion Models (AMDM). The algorithm integrates features from multiple diffusion models into a specified model to activate particular features and enable fine-grained control. Experimental results demonstrate that AMDM significantly improves fine-grained control without training, validating its effectiveness. Additionally, it reveals that diffusion models initially focus on features such as position, attributes, and style, with later stages improving generation quality and consistency. AMDM offers a new perspective for tackling the challenges of fine-grained conditional generation in diffusion models. Specifically, it allows us to fully utilize existing or develop new conditional diffusion models that control specific aspects, and then aggregate them using the AMDM algorithm. This eliminates the need for constructing complex datasets, designing intricate model architectures, and incurring high training costs. Code is available at: <https://github.com/Hammour-steak/AMDM>.

1 INTRODUCTION

Diffusion models (Sohl-Dickstein et al., 2015; Ho et al., 2020; Song et al., 2021a;b; Karras et al., 2022) have achieved excellent performance in generative tasks. In particular, conditional diffusion models (Rombach et al., 2022; Chung et al., 2023; Esser et al., 2024) not only deliver advanced results in practical applications such as Text-to-Image (Nichol et al., 2022; Chen et al., 2023; Lee et al., 2024; Xu et al., 2024) and Image-to-Image generation (Zhang et al., 2023; Mou et al., 2024), but also offer highly flexible conditional control mechanisms.

Recent research on conditional diffusion models has focused on achieving fine-grained control, including object attributes (Wu et al., 2023; Wang et al., 2024a), interactions (Hoe et al., 2024; Jia et al., 2024), layouts (Zheng et al., 2023; Chai et al., 2023; Chen et al., 2024b), and style (Wang et al., 2023; Huang et al., 2024; Qi et al., 2024). However, maintaining consistency across diverse nuanced control remains a significant challenge. Generating multiple objects with overlapping bounding boxes can lead to attribute leakage, where the description of one object inappropriately influences others, causing inconsistencies between objects and the background. Fine-grained interaction details may be illogical, and style integration may compromise object attributes.

Existing approaches only partially address these issues due to the inherent complexity and diversity of fine-grained control, coupled with limitations in datasets and model architectures. Some works (Li et al., 2023; Zhou et al., 2024; Wang et al., 2024b) may perform well in preventing attribute leakage among multiple instances during layout generation but perform poorly in managing object

*Corresponding Author

interactions, while others (Ye et al., 2023; Huang et al., 2024) may excel in style transfer but exhibit limited control over layout.

Interestingly, most of these methods are based on Stable Diffusion (Rombach et al., 2022), which is theoretically grounded in DDPM (Ho et al., 2020) and classifier-free guidance (Dhariwal & Nichol, 2021) for conditional control. Therefore, for these conditional diffusion models that are grounded in the same theoretical foundation, our objective is to overcome this challenge by developing a method that effectively aggregates the advantages of each model, leveraging their unique strengths to achieve fine-grained control.

This paper makes the following contributions: **(1)** proposes a novel diffusion model aggregation algorithm, AMDM, that can aggregate intermediate variables from multiple conditional diffusion models with a shared encoder and diffusion process, independent of the denoising network architecture, absorbing the characteristics of each model and enabling fine-grained generation; **(2)** conducts extensive experiments, with both qualitative and quantitative results demonstrating significant improvements, particularly in regions where previous models exhibited limited controllability, thereby validating the effectiveness of AMDM; **(3)** reveals that diffusion models initially focus on generating coarse-grained features such as position, attributes, and style, while later stages emphasize quality and consistency, implying that aggregation algorithms can be applied only in the first s steps, substantially reducing computational overhead.

2 PRELIMINARIES

2.1 DIFFUSION MODELS

Diffusion models are a class of generative models that progressively add noise to guide the data distribution $q(\mathbf{x}_0)$ towards a Gaussian distribution. In the classical DDPM (Ho et al., 2020) formulation, the noise addition process from time $t-1$ to t is defined as:

$$q(\mathbf{x}_t | \mathbf{x}_{t-1}) = \mathcal{N}(\sqrt{\alpha_t} \mathbf{x}_{t-1}, (1 - \alpha_t) \mathbf{I}), \quad (1)$$

where \mathbf{x}_t represents the noisy data at timestep $t \in [0, T]$, α_t is the coefficient drift schedule generally satisfying $\lim_{t \rightarrow T} \alpha_t = 0$. From (1), we can readily derive the forward marginal distribution:

$$q(\mathbf{x}_t | \mathbf{x}_0) = \mathcal{N}(\sqrt{\bar{\alpha}_t} \mathbf{x}_0, (1 - \bar{\alpha}_t) \mathbf{I}), \quad (2)$$

where $\bar{\alpha}_t = \prod_{i=1}^t \alpha_i$. The forward process (2) indicates that we can directly obtain \mathbf{x}_t from \mathbf{x}_0 avoiding multistep sampling. Assuming the generative model is $p_\theta(x_0)$, consider the variational lower bound of its likelihood as the loss function, i.e., the KL divergence of the joint probability:

$$\mathcal{L} = KL(q(\mathbf{x}_{0:T}) \| p_\theta(\mathbf{x}_{0:T})) \propto \mathbb{E}_{t, \mathbf{x}_t, \epsilon_t} [\|\epsilon_t - \epsilon_\theta(\mathbf{x}_t, t)\|^2], \quad (3)$$

where $\epsilon_t \sim \mathcal{N}(\mathbf{0}, \mathbf{I})$ and $\epsilon_\theta(\mathbf{x}_t, t)$ is the denoising neural network. More generally, we utilize DDIM (Song et al., 2021a) sampling which directly defines the forward process (2) compared to DDPM. Ultimately, the reverse sampling process is as follows:

$$p_\theta(\mathbf{x}_{t-1} | \mathbf{x}_t) = \mathcal{N} \left(\sqrt{\frac{\bar{\alpha}_{t-1}}{\bar{\alpha}_t}} \mathbf{x}_t + \left(\sqrt{1 - \bar{\alpha}_{t-1} - \sigma_t^2} - \sqrt{\frac{\bar{\alpha}_{t-1}(1 - \bar{\alpha}_t)}{\bar{\alpha}_t}} \right) \epsilon_\theta(\mathbf{x}_t, t), \sigma_t^2 \mathbf{I} \right), \quad (4)$$

where σ_t is a free variable. When $\sigma_t^2 = \frac{1 - \bar{\alpha}_{t-1}}{1 - \bar{\alpha}_t} (1 - \frac{\bar{\alpha}_t}{\bar{\alpha}_{t-1}})$, it corresponds to DDPM sampling, while $\sigma_t^2 = 0$ results in a deterministic sampling, which is the origin of the name DDIM.

In practical applications, to reduce the computational cost of training and inference, an increasing number of diffusion models perform the diffusion process in the latent space. Among them, the most representative is Stable Diffusion (Rombach et al., 2022), which employs a Variational Autoencoder (VAE) (Kingma & Welling, 2013) to map the data distribution into a latent distribution and defines the diffusion process within this latent space.

2.2 CLASSIFIER-FREE GUIDANCE

The key to conditional control in diffusion models is estimating $q(\mathbf{x}_{t-1} | \mathbf{x}_t, y)$ given the condition y . In unconditional generation, according to (4), it can be written as:

$$p_\theta(\mathbf{x}_{t-1} | \mathbf{x}_t) = \mathcal{N}(\mu_\theta(\mathbf{x}_t, t), \sigma_t^2 \mathbf{I}). \quad (5)$$

Accordingly, Classifier-Free Guidance (Dhariwal & Nichol, 2021) directly incorporates the condition y into the mean for estimation:

$$\begin{aligned} p_\theta(\mathbf{x}_{t-1} \mid \mathbf{x}_t, y) &= \mathcal{N}(\boldsymbol{\mu}_\theta(\mathbf{x}_t, t, y), \sigma_t^2 \mathbf{I}) \\ &= \mathcal{N}\left(\sqrt{\frac{\bar{\alpha}_{t-1}}{\bar{\alpha}_t}} \mathbf{x}_t + \left(\sqrt{1 - \bar{\alpha}_{t-1} - \sigma_t^2} - \sqrt{\frac{\bar{\alpha}_{t-1}(1 - \bar{\alpha}_t)}{\bar{\alpha}_t}}\right) \boldsymbol{\epsilon}_\theta(\mathbf{x}_t, t, y), \sigma_t^2 \mathbf{I}\right), \end{aligned} \quad (6)$$

and the training loss function is:

$$\mathcal{L} \propto \mathbb{E}_{t, \mathbf{x}_t, \boldsymbol{\epsilon}_t} [\|\boldsymbol{\epsilon}_t - \boldsymbol{\epsilon}_\theta(\mathbf{x}_t, t, y)\|^2]. \quad (7)$$

The noise model $\boldsymbol{\epsilon}_\theta(\mathbf{x}_t, t, y)$ incorporates conditioning on y , guiding the denoising process towards the conditioned direction, thereby enabling conditional sampling and generation.

3 AMDM

In this section, we first analyze the challenges and limitations of current fine-grained control research, and establish the existence and applicability of aggregation algorithms. We then describe the design principles and propose the final algorithm, AMDM.

3.1 ANALYSIS

Current fine-grained conditional control models tend to have limited control capabilities and face numerous issues. For example, given the caption "A red hair girl is drinking from a blue bottle of water, oil painting" and corresponding bounding boxes for positioning control, different models are likely to show varying performance, as illustrated in Figure 1. Model A, which receives additional inputs for position information and actions, excels in generating high-quality generation of positioning and interactions. However, it struggles with attribute control and maintaining the oil painting style. Conversely, Model B incorporates extra input for position and attribute information, managing both but not accurately capturing interactions and stylistic elements. Model C references the style of an image, enabling precise management of style characteristics but lacking adequate control over location and attribute details. The fundamental reason for these issues lies in the complexity and flexibility of fine-grained control tasks, which makes it challenging for limited datasets and specific model architectures to account for all the intricate features. Although implementing a specific feature for a particular task is relatively straightforward, integrating these features for fine-grained control remains a significant challenge.

While different models may have varying additional input conditions, these conditions are often mutually compatible, leading to consistent objectives, which allows the models to generate similar images within their respective generation domains. Theoretically, model A has the capability to generate images that meet all the composite conditions of the caption for fine-grained control, although a single sampling might not fully activate this capability. It is noteworthy that these models share a common theoretical foundation, as they are all predicated on the same diffusion process and Classifier-Free Guidance (CFG) conditional control mechanism. Recognizing this shared basis, our objective is to develop an aggregation algorithm that leverages these commonalities to integrate the distinctive characteristics of multiple models into a specific model, achieving fine-grained conditional control in a more direct and efficient manner.

Do aggregation operations exist in different diffusion models? For a latent diffusion model p_θ , we define the encoder by $z_0 = E(x_0)$. The true data manifold along the diffusion process is defined as $\mathcal{M}_t(\xi_t) = \{\mathbf{z}_t \in \mathbb{R}^n \mid p(\mathbf{z}_t) \geq \xi_t\}$, where an appropriate choice of ξ_t ensures that \mathcal{M}_t is a set of meaningful data. Furthermore, we define the generation domain at time t under condition y as $D_{t,y}^\theta(\tau_{t,y}^\theta) = \{\mathbf{z}_t \in \mathbb{R}^n \mid p_\theta(\mathbf{z}_t \mid y) \geq \tau_{t,y}^\theta\}$. Since conditional samples are a selection of



Figure 1: Examples of fine-grained conditional control of the same caption by different models.

the unconditional population, there exists a largest threshold $\tau_{t,y}^\theta$ such that $D_{t,y}^\theta(\tau_{t,y}^\theta) \subset \mathcal{M}_t(\xi_t)$. This implies that, given ξ_t , the $D_{t,y}^\theta(\tau_{t,y}^\theta)$ is uniquely determined; hence, for simplicity, we can omit the explicit dependence on the threshold. Mathematically, the most fundamental requirement for performing aggregation operations is that all elements must reside in a shared space. However, in the case of aggregation between two models, it is evident that data obtained through conditional sampling from Model 1 should lie within $D_{0,y_1}^{\theta_1}$, whereas data obtained from Model 2 should lie within $D_{0,y_2}^{\theta_2}$. According to the definition, $D_{0,y_1}^{\theta_1} \subset \mathcal{M}_0$, $D_{0,y_2}^{\theta_2} \subset \mathcal{M}_0$, which implies that the data from different models can be embedded into a shared representation space \mathcal{M}_0 . This observation directly leads to the **first requirement**: \mathcal{M}_0 must coincide across models, implying that the latent space encoders are consistent, and the aggregation operations at $t = 0$ exists. For $t > 0$, this naturally leads to the **second requirement**: \mathcal{M}_t must coincide across models. In the context of diffusion models, a sufficient condition for this requirement is that the underlying SDEs are identical. Consequently, we obtain $D_{t,y_1}^{\theta_1}, D_{t,y_2}^{\theta_2} \subset \mathcal{M}_t$, which ensures the existence of aggregation operations for all time steps t .

Which models can achieve fine-grained generation through aggregation operations? In practice, we expect the result of the operation to lie within the smaller space $D_{t,y_1}^{\theta_1} \cap D_{t,y_2}^{\theta_2}$, since only in this space is it possible to faithfully incorporate information from both models and achieve fine-grained generation. In order to achieve aggregation operation at time t , it is further required that the domains $D_{t,y_1}^{\theta_1}$ and $D_{t,y_2}^{\theta_2}$ of different models possess a non-empty intersection. Fortunately, in fine-grained generation tasks, the intersection naturally exists for **almost all** applicable models. This is because both models share the same generation target in fine-grained tasks, meaning the conditions y_1 and y_2 are compatible, and the data generated by both models tend to be similar, i.e., $D_{0,y_1}^{\theta_1} \cap D_{0,y_2}^{\theta_2} \neq \emptyset$, and for the noised state at any time t , we similarly have $D_{t,y_1}^{\theta_1} \cap D_{t,y_2}^{\theta_2} \neq \emptyset$.

The above analysis indicates that there exists an appropriate aggregation algorithm that can achieve fine-grained generation in almost all practical models with consistent encoders and a diffusion process. Beyond the case of two models, it can also naturally extends to multiple models, thereby providing a solid foundation for the design of the subsequent algorithm.

3.2 ALGORITHM

Spherical Aggregation. To identify a feasible aggregation algorithm, we need to examine the properties of \mathcal{M}_t . First, general latent diffusion models such as Stable Diffusion (Rombach et al., 2022) typically employ a VAE (Kingma & Welling, 2013) to map the data distribution $p(\mathbf{x}_0)$ into a latent distribution $p(\mathbf{z}_0)$. In theory, according to the definition of VAE, $p(\mathbf{z}_0)$ should approximate a standard Gaussian distribution. However, in practice, the weight of the KL divergence term in the VAE loss function is usually set to be very small, which makes the VAE primarily as an efficient encoder rather than a fully generative model. Consequently, the main role of the VAE in SD is to perform dimensionality reduction, accelerating both training and inference. As a result, the latent distribution $p(\mathbf{z}_0)$ still exhibits a complex structure instead of strictly following a Gaussian distribution. For the diffusion process from a general distribution $p(\mathbf{z}_0)$ to the Gaussian prior $p(\mathbf{z}_T)$, Chung et al. (2022) demonstrated that \mathcal{M}_t is concentrated on an $(n - 1)$ -dimensional manifold, which approximates an n -dimensional hypersphere as t becomes large. This motivates the use of spherical linear interpolation as the aggregation operation when t is large, which maximizes the retention of the aggregated data on the original manifold while minimizing deviations. Therefore, the aggregation operation of the two models θ_1, θ_2 is defined as:

$$\begin{aligned} \mathbf{z}'_{t-1} &= Slerp(\mathbf{z}_{t-1}^{\theta_1}, \mathbf{z}_{t-1}^{\theta_2}, w) \\ &= \frac{\sin((1-w)\varphi)}{\sin(\varphi)} \mathbf{z}_{t-1}^{\theta_1} + \frac{\sin(w\varphi)}{\sin(\varphi)} \mathbf{z}_{t-1}^{\theta_2}, \\ \varphi &= \cos^{-1}(\mathbf{z}_{t-1}^{\theta_1} \cdot \mathbf{z}_{t-1}^{\theta_2}), \end{aligned} \tag{8}$$

where \mathbf{z}'_{t-1} represents the aggregated intermediate variable, $\mathbf{z}_{t-1}^{\theta_1}, \mathbf{z}_{t-1}^{\theta_2}$ are sampled from $p_{\theta_1}(\mathbf{z}_{t-1}^{\theta_1} | \mathbf{z}_t^{\theta_1}, y_1), p_{\theta_2}(\mathbf{z}_{t-1}^{\theta_2} | \mathbf{z}_t^{\theta_2}, y_2)$ respectively, and $w \in [0, 1]$ is the weighting factor that balances the contribution of each model. Spherical aggregation integrates the conditional control information of p_{θ_2} into p_{θ_1} , while keeping the new variables stable near the manifold.

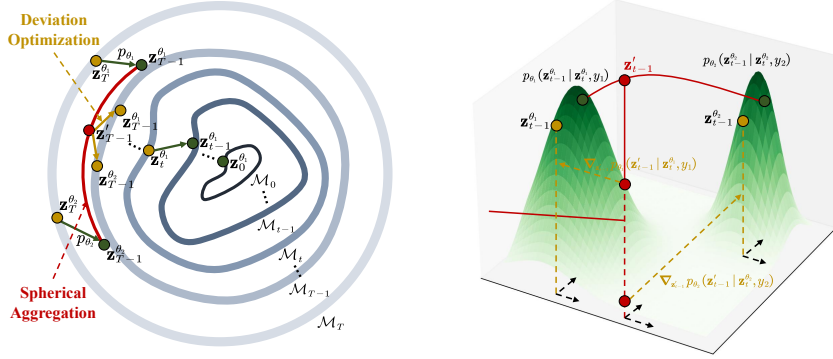


Figure 2: Geometry of AMDM (Left) and Deviation Optimization (Right). The algorithm employs spherical aggregation and deviation optimization to incorporate conditional information during the initial steps. Subsequently, direct sampling is applied to expedite the process and generate high-quality images.

Deviation Optimization. Ideally, we expect $\mathbf{z}'_{t-1} \in D_{t-1, y_1}^{\theta_1} \cap D_{t-1, y_2}^{\theta_2}$, but deviations are likely to occur in practice. Considering the step from t to $t-1$, since $p_{\theta_1}(\mathbf{z}_{t-1}^{\theta_1} | \mathbf{z}_t^{\theta_1}, y_1)$ is high-dimensional Gaussian, its samples concentrate in a thin spherical shell around the mean. Motivated by this, we perform a radial adjustment of \mathbf{z}'_{t-1} toward that shell to obtain $\tilde{\mathbf{z}}_{t-1} \in D_{t-1, y_1}^{\theta_1}$. This adjustment alone does not guarantee $\tilde{\mathbf{z}}_{t-1} \in D_{t-1, y_2}^{\theta_2}$. Nevertheless, we show that $\tilde{\mathbf{z}}_{t-1}$ belongs to $D_{t-1, y_2}^{\theta_2}$ with high probability, which leads to the following proposition:

Proposition 3.1. *For the diffusion model p_{θ_1} defined by (6) and any new intermediate variable \mathbf{z}'_{t-1} from (8), let:*

$$\tilde{\mathbf{z}}_{t-1} = \mathbf{z}'_{t-1} - \eta_{t-1}^{\theta_1} \frac{\mathbf{z}'_{t-1} - \mu_{\theta_1}(\mathbf{z}_t^{\theta_1}, t, y_1)}{\|\mathbf{z}'_{t-1} - \mu_{\theta_1}(\mathbf{z}_t^{\theta_1}, t, y_1)\|}, \quad (9)$$

where $\eta_{t-1}^{\theta_1}$ is a small optimization step size. There exists $\eta_{t-1}^{\theta_1}$ such that $\tilde{\mathbf{z}}_{t-1} \in D_{t-1, y_1}^{\theta_1}$. Moreover, an approximate lower bound on the probability that $\tilde{\mathbf{z}}_{t-1} \in D_{t-1, y_2}^{\theta_2}$ is given by:

$$P\left(\tilde{\mathbf{z}}_{t-1} \in D_{t-1, y_2}^{\theta_2}\right) \geq 1 - 2 \exp\left(-\frac{n \left(\epsilon_{t-1}^{\theta_2} - \frac{d}{\sigma_t \sqrt{n}}\right)^2}{1 + 2 \left(\epsilon_{t-1}^{\theta_2} - \frac{d}{\sigma_t \sqrt{n}}\right)}\right), \quad (10)$$

where $d = \phi_w(\varphi) \|\mathbf{z}_{t-1}^{\theta_1} - \mathbf{z}_{t-1}^{\theta_2}\| + \eta_{t-1}^{\theta_1}$ and $\phi_w(\varphi) = \sin((1-w)\varphi/2) / \sin(\varphi/2)$.

The proof is given in Appendix B; a detailed analysis of d is presented in Appendix C.3; and the geometry of deviation optimization is illustrated in Figure 2 (Right). Proposition 3.1 shows that $\tilde{\mathbf{z}}_{t-1}$ obtained after spherical aggregation can be corrected into $D_{t-1, y_1}^{\theta_1}$ through deviation optimization, and with high probability can also be corrected into $D_{t-1, y_2}^{\theta_2}$. This not only improves the quality of sampling but also establishes that the new variable is able to simultaneously capture information from both models.

Combining equations (8) and (9), the algorithm for aggregation of two diffusion models is presented, comprising two key components: spherical aggregation and deviation optimization. Spherical aggregation aggregates the conditional control information from different models and ensures that the new intermediate variables remain stable near the manifold, while deviation optimization ensures more precise retention on the corresponding data manifold, enhancing sample quality. The algorithm iteratively performs spherical aggregation and deviation optimization for each model during the first s steps, followed by direct sampling from p_{θ_1} . This algorithm can be readily extended to multiple models, resulting in the final Aggregation of Multiple Diffusion Models (AMDM) algorithm, as shown in Algorithm 1 and Figure 2 (Left), where the spherical aggregation of multiple elements is defined through successive pairwise aggregation.

Algorithm 1 AMDM

Input: models $p_{\theta_1}, p_{\theta_2}, \dots, p_{\theta_N}$, conditions y_1, y_2, \dots, y_N , aggregation step s , weighting factor w_1, w_2, \dots, w_{N-1} and optimization step $\eta_t^{\theta_1}, \eta_t^{\theta_2}, \dots, \eta_t^{\theta_N}$
 $\mathbf{z}_T^{\theta_1}, \mathbf{z}_T^{\theta_2}, \dots, \mathbf{z}_T^{\theta_N} \sim N(\mathbf{0}, \mathbf{I})$
for t in $[T : 1]$ **do**
 $\mathbf{z}_{t-1}^{\theta_1} \sim p_{\theta_1}(\mathbf{z}_{t-1}^{\theta_1} | \mathbf{z}_t^{\theta_1}, y_1)$
if $t > T - s$ **then**
 $\mathbf{z}_{t-1}^{\theta_i} \sim p_{\theta_i}(\mathbf{z}_{t-1}^{\theta_i} | \mathbf{z}_t^{\theta_i}, y_i), i \in [2, N]$
 $\mathbf{z}'_{t-1} = Slerp(\mathbf{z}_{t-1}^{\theta_1}, \dots, \mathbf{z}_{t-1}^{\theta_N}, w_1, \dots, w_{N-1})$
 $\mathbf{z}_{t-1}^{\theta_i} = \mathbf{z}'_{t-1} - \eta_t^{\theta_i} \frac{\mathbf{z}'_{t-1} - \mu_{\theta_i}(\mathbf{z}_t^{\theta_i}, t, y_i)}{\|\mathbf{z}'_{t-1} - \mu_{\theta_i}(\mathbf{z}_t^{\theta_i}, t, y_i)\|}, i \in [1, N]$
end if
end for
 $\mathbf{x}_0^{\theta_1} = \text{Decoder}(\mathbf{z}_0^{\theta_1})$
Output: $\mathbf{x}_0^{\theta_1}$

We perform aggregation only in the first s steps, and subsequently apply a single model p_{θ_1} for inference. This procedure can be regarded as aggregating the features of other models into p_{θ_1} , striking a balance between efficiency and effectiveness. Moreover, note that since $\mu_{\theta_i}(\mathbf{z}_t^{\theta_i}, t, y_i)$ can reuse $\epsilon_{\theta_i}(\mathbf{z}_t^{\theta_i}, t, y_i)$ from the previous sampling step, the deviation optimization introduces only a single mathematical operation with negligible computational overhead, further reducing inference time.

As for the selection of p_{θ_1} , in order to ensure high-quality generation in the later stages, it is natural to choose the model with stronger generative capability as p_{θ_1} . This choice can be evaluated using a variety of criteria, such as quantitative metrics, model size, application universality, or direct experimental validation.

4 EXPERIMENTS

In this section, we aggregate several classic conditional diffusion models, all of which are based on SD and satisfy the AMDM requirements of a shared encoder and identical SDE, followed by a series of ablation experiments to demonstrate its optimality. The core idea of our experiment is to demonstrate the effectiveness of the AMDM algorithm as follows: Given a set of models with varying control capabilities, we only need to focus on whether the target model, after aggregating features from other models, can enhance its performance in areas of weak control, reaching the level of the stronger models, while simultaneously preserving its own control advantages. All experiments were conducted using a single RTX 3090 GPU and experimental details and additional experiments are provided in Appendix D.

4.1 AGGREGATION EXPERIMENTS

InteractDiffusion and MIGC. InteractDiffusion (Hoe et al., 2024) is a T2I model that combines a pretrained Stable Diffusion (SD) model with a locally controlled interaction mechanism, enabling fine-grained control over the generated images and demonstrating effective interactivity. MIGC (Zhou et al., 2024) is a T2I model that employs a divide-and-conquer strategy, achieving excellent performance in both attribute representation and isolation of generated instances. InteractDiffusion primarily focuses on controlling subject-object interactions. However, due to the lack of explicit constraints on object attributes within the model architecture and dataset design, it exhibits suboptimal performance in attribute control. To address this, we attempt to aggregate the features of MIGC p_{θ_2} into

Table 1: Quantitative results on the HOI Detection Score, FID and CLIP Score across different models.

Method	Default \uparrow		Known Object \uparrow		FID \downarrow	CLIP Score \uparrow
	Full	Rare	Full	Rare		
MIGC	16.87	18.05	17.84	19.02	30.53	27.36
MIGC+InteractDiffusion	26.04	21.73	27.02	22.89	22.32	27.55
InteractDiffusion	29.53	23.02	30.99	24.93	18.69	26.91
InteractDiffusion+MIGC	31.40	24.52	32.76	26.32	18.35	27.18

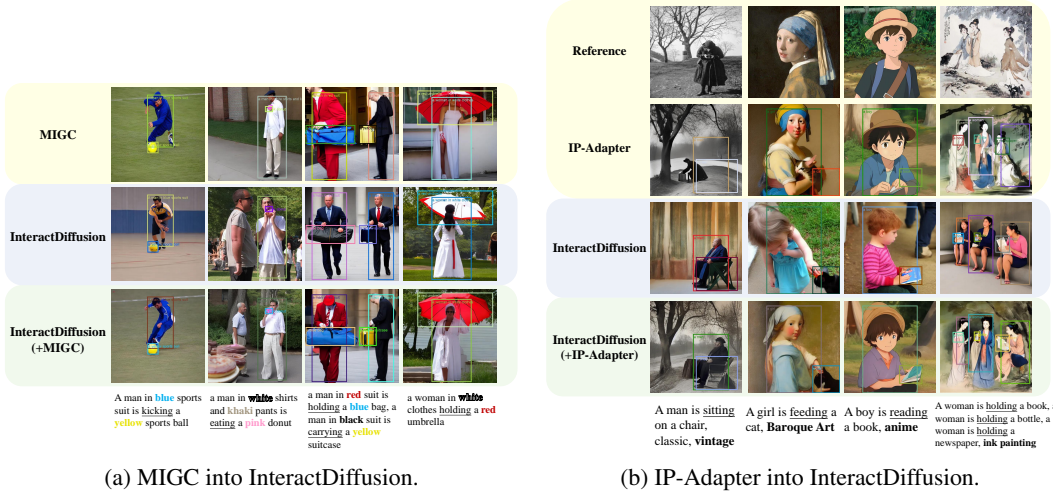


Figure 3: Visual results of applying AMDM algorithm.

Table 2: Quantitative results on the COCO-MIG benchmark and CLIP Score across different models.

Method	Instance Success Rate (%) ↑						mIoU Score (%) ↑						CLIP Score ↑	
	L_2	L_3	L_4	L_5	L_6	Avg	L_2	L_3	L_4	L_5	L_6	Avg	Global	Local
InteractDiffusion	37.50	35.62	35.31	30.62	34.16	34.06	32.98	31.63	30.82	28.29	30.40	30.40	31.09	27.56
InteractDiffusion(+MIGC)	62.29	54.33	56.31	53.87	52.89	54.78	54.30	46.37	48.44	47.65	46.64	47.74	32.81	28.96
MIGC	64.06	56.04	58.43	56.00	49.89	55.46	54.43	49.33	50.48	48.67	44.74	48.53	32.78	28.61
MIGC(+InteractDiffusion)	60.00	50.20	50.46	48.25	46.97	49.78	52.58	44.27	43.39	42.67	41.50	43.69	32.41	28.55

InteractDiffusion p_{θ_1} by applying the AMDM algorithm, introducing attribute control information, and denoting this as InteractDiffusion(+MIGC).

Visual results are shown in Figure 3a. It is evident that aggregating the MIGC model into InteractDiffusion using our proposed AMDM algorithm significantly enhances its learned representations, leading to a notable improvement in instance attribute control, and confirming the algorithm’s effectiveness.

MIGC demonstrates strong attribute control on the COCO-MIG benchmark (Zhou et al., 2024), while InteractDiffusion mainly uses the FGAHOI (Ma et al., 2023) for Human-Object Interaction (HOI) detection to show its control over interaction. To further validate the effectiveness of AMDM, we evaluate whether MIGC(+InteractDiffusion) can retain attribute control on COCO-MIG while significantly enhancing HOI interaction, ideally reaching the performance level of InteractDiffusion. Conversely, we also examine whether InteractDiffusion(+MIGC) can preserve interaction control while improving attribute control to match that of MIGC.

The quantitative results of InteractDiffusion(+MIGC) are shown in the first two rows of Table 2. It can be observed that all metrics have significantly improved in InteractDiffusion(+MIGC) in attribute control. Interestingly, as shown in the last two rows of Table 1, it even surpasses the original InteractDiffusion model in terms of interaction. Similarly, the results of MIGC(+InteractDiffusion) are shown in the first two rows of Table 1. It can be seen that MIGC(+InteractDiffusion) also shows significant improvements across all metrics in the interaction capability control. Additionally, as observed in the last two rows of Table 2, the MIGC(+InteractDiffusion) maintains the original performance of MIGC in attribute control, validating the effectiveness of the algorithm.

InteractDiffusion and IP-Adapter. IP-Adapter (Ye et al., 2023) is a lightweight I2I model that employs a decoupled cross-attention mechanism to separately process text and image features, enabling multimodal image generation. Due to its superior performance in preserving the style of the reference image, we propose integrating the style information from IP-Adapter p_{θ_3} into InteractDiffusion p_{θ_1} , denoted as InteractDiffusion(+IP-Adapter). The experimental results are shown in Figure 3b. It can be observed that IP-Adapter enhances the style representations of InteractDiffusion, fully activating its style controllability, which further validates the effectiveness of the algorithm.

InteractDiffusion, MIGC and IP-Adapter. Furthermore, we attempt to aggregate the attribute features from MIGC p_{θ_2} and the style features from IP-Adapter p_{θ_3} into InteractDiffusion p_{θ_1} to evaluate the effectiveness of the AMDM algorithm. The experimental results are presented in Figure 4.

4.2 ABLATION STUDIES

We first attempt a comparison with linear aggregation of InteractDiffusion(+MIGC) which has been of broad interest in compositional generation and the results are shown in the Figure 5a. It can be observed that when the number of aggregation steps is small ($s < 5$), linear aggregation performs slightly better than spherical aggregation. However, as the number of aggregation steps increases, spherical aggregation significantly outperforms linear aggregation across various metrics. This is because, with more aggregation steps, the cumulative error due to the deviation in the data manifold becomes increasingly larger in linear aggregation, which negatively impacts the image quality. As shown in Figure 5b, the characteristic of manifold deviation in linear aggregation is evident. In contrast, spherical aggregation consistently minimizes the deviation of the aggregated variables from the spherical manifold, preserving the quality of the final image as much as possible. The deviation optimization further enhances the image quality, demonstrating its effectiveness. A more detailed discussion of linear compositional methods can be found in the Related Work and Appendix E.

Moreover, as shown in Figure 5a, the effectiveness of spherical aggregation consistently increases over time and remains almost entirely on the manifold. This is because, when t is relatively small, although \mathcal{M}_t is no longer approximately Gaussian, the conditions $\|\mathbf{z}_t^{\theta_1}\| \approx \|\mathbf{z}_t^{\theta_2}\|$ and $\varphi \approx 0$ imply that $\mathbf{z}_t^{\theta_1}$ and $\mathbf{z}_t^{\theta_2}$ lie on a local sphere, which corresponds to an isotropic Gaussian distribution. Consequently, spherical aggregation still preserves the manifold structure, which reveals the fundamental reason behind the success of AMDM. A detailed analysis of the conditions is provided in Appendix C.2 and C.3.

We also investigated the optimization step of deviation optimization, with experimental results shown in Table 4. Obviously, when the optimization step is set to 0.3, the best performance is achieved across all metrics. Moreover, the results outperform those achieved with 50 aggregation steps without optimization.

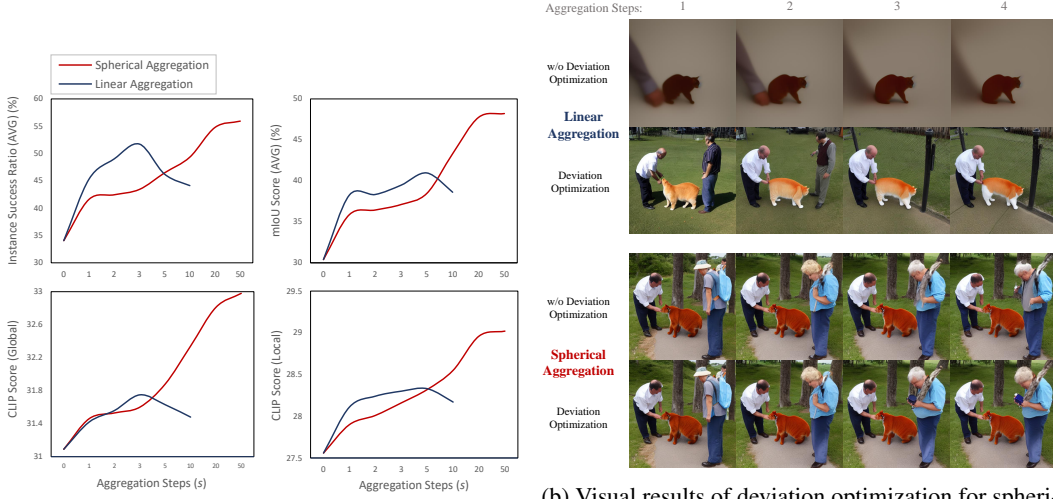
Finally, we conduct ablation studies on the aggregation at different stages of the AMDM algorithm. As shown in Table 3, the best results are achieved when aggregation occurs during the initial stages of sampling. At other stages, especially the final ones, leads to a noticeable drop in generation quality, with weaker control over attributes and interactions. This further supports the claim that diffusion models initially focus on generating features such as position, attributes, and style, while later stages emphasize quality and consistency.



Figure 4: Visual results of aggregating MIGC and IP-Adapter into InteractDiffusion.

Table 3: InteractDiffusion(+MIGC) with total 20 steps sampling and $s=10$.

Aggregation Stage	ISR (avg) \uparrow	Default (Full) \uparrow	FID \downarrow
$t_{20} \rightarrow t_{10}$	54.78	31.40	18.35
$t_{15} \rightarrow t_5$	46.23	26.21	54.61
$t_{10} \rightarrow t_0$	41.65	23.47	74.53



(a) Metrics of spherical aggregation and linear aggregation under different aggregation steps.

(b) Visual results of deviation optimization for spherical aggregation and linear aggregation under different aggregation steps.

Figure 5: Ablation study.

Table 4: Ablation results of different deviation optimization step on COCO-MIG benchmark in InteractDiffusion(+MIGC).

Deviation Optimization Step	Instance Success Rate (%) ↑						mIoU Score (%) ↑						CLIP Score ↑	
	L_2	L_3	L_4	L_5	L_6	Avg	L_2	L_3	L_4	L_5	L_6	Avg	Global	Local
0	61.56	52.08	53.75	51.62	51.87	53.18	54.76	45.09	46.36	45.48	45.79	46.62	31.09	27.56
0.1	57.60	53.26	53.89	52.40	52.08	53.26	53.27	45.53	46.86	46.31	45.80	46.83	31.43	27.87
0.2	59.62	54.27	54.06	51.25	52.29	53.40	52.71	46.32	47.17	44.68	45.74	46.59	31.92	28.45
0.3	62.29	54.33	56.31	53.87	52.89	54.78	54.30	46.37	48.44	47.65	46.64	47.74	32.81	28.96
0.4	61.34	53.62	55.32	52.22	52.50	53.96	53.46	46.21	46.82	45.26	46.23	46.78	32.23	28.55
0.5	58.30	53.43	55.14	51.76	51.76	53.27	52.88	45.03	46.52	44.95	45.51	46.14	31.15	27.78

5 RELATED WORKS

Fine-Grained Generation. Beyond text-driven models (Nichol et al., 2022; Ramesh et al., 2022; Li et al., 2024b; Podell et al., 2024), research is increasingly moving toward finer-grained conditional control. A classical route is personalization-controlled generation—covering style (Sohn et al., 2023; Hertz et al., 2024; Chen et al., 2024a), subject (Li et al., 2024a; Shi et al., 2024; Jiang et al., 2024; Ye et al., 2023), person (Xiao et al., 2024; Giambi & Lisanti, 2023; Peng et al., 2024), and interactive generation (Huang et al., 2023b; Guo et al., 2024; Hoe et al., 2024). Another focus is spatial control (Li et al., 2023; Cheng et al., 2023; Nie et al., 2024; Zhou et al., 2024), which uses bounding boxes or regions as additional conditions to enforce spatial constraints. More recently, several studies have pursued direct fine-grained multimodal control (Huang et al., 2023a; Smith et al., 2023; Gu et al., 2024; Kumari et al., 2023), but these approaches typically require extensive multi-condition datasets and increasingly complex model architectures.

Compositional Generation. Some recent works (Du et al., 2020; Liu et al., 2022; Du et al., 2023; Du & Kaelbling, 2024; Garipov et al., 2023; Bradley et al., 2025; Thornton et al., 2025; Skreta et al., 2025a; He et al., 2025; Skreta et al., 2025b) aim to create new distributions by combining different distributions, commonly using techniques such as linear weighted score, followed by simulated annealing or other optimization methods. Other works (Biggs et al., 2024; Oh et al., 2025; Wang et al., 2025) attempt to combine models by applying weighted interpolation to their parameters. However, this approach requires that the models share an identical architecture, which significantly restricts its applicability. A more in-depth comparison of our AMDM and its relation to compositional generation methods can be found in the Appendix E.

6 CONCLUSION

This paper proposes a novel AMDM algorithm designed for fine-grained generation, which consists of two main components: spherical aggregation and deviation optimization. Experimental results demonstrate the effectiveness of the AMDM algorithm, revealing that diffusion models initially prioritize image feature generation, shifting their focus to image quality and consistency in later stages. The algorithm provides a new perspective for addressing fine-grained generation challenge: We can leverage existing or develop new conditional diffusion models that control specific aspects, and then aggregate them using the AMDM algorithm. This eliminates the need for constructing complex datasets, designing intricate model architectures, and incurring high training costs.

REFERENCES

Benjamin Biggs, Arjun Seshadri, Yang Zou, Achin Jain, Aditya Golatkar, Yusheng Xie, Alessandro Achille, Ashwin Swaminathan, and Stefano Soatto. Diffusion soup: Model merging for text-to-image diffusion models. In *European Conference on Computer Vision*, pp. 257–274. Springer, 2024.

Arwen Bradley, Preetum Nakkiran, David Berthelot, James Thornton, and Joshua M Susskind. Mechanisms of projective composition of diffusion models. *arXiv preprint arXiv:2502.04549*, 2025.

Shang Chai, Liansheng Zhuang, and Fengying Yan. Layoutdm: Transformer-based diffusion model for layout generation. In *Proceedings of the IEEE/CVF Conference on Computer Vision and Pattern Recognition*, pp. 18349–18358, 2023.

Dar-Yen Chen, Hamish Tennent, and Ching-Wen Hsu. Artadapter: Text-to-image style transfer using multi-level style encoder and explicit adaptation. In *Proceedings of the IEEE/CVF Conference on Computer Vision and Pattern Recognition*, pp. 8619–8628, 2024a.

Jingye Chen, Yupan Huang, Tengchao Lv, Lei Cui, Qifeng Chen, and Furu Wei. Textdiffuser: Diffusion models as text painters. *Advances in Neural Information Processing Systems*, 36, 2024b.

Wenhu Chen, Hexiang Hu, Chitwan Saharia, and William W Cohen. Re-imagen: Retrieval-augmented text-to-image generator. In *The Eleventh International Conference on Learning Representations*, 2023.

Jiaxin Cheng, Xiao Liang, Xingjian Shi, Tong He, Tianjun Xiao, and Mu Li. Layoutdiffuse: Adapting foundational diffusion models for layout-to-image generation. *arXiv preprint arXiv:2302.08908*, 2023.

Hyungjin Chung, Byeongsu Sim, Dohoon Ryu, and Jong Chul Ye. Improving diffusion models for inverse problems using manifold constraints. In *Advances in Neural Information Processing Systems*, 2022.

Hyungjin Chung, Jeongsol Kim, Michael Thompson Mccann, Marc Louis Klasky, and Jong Chul Ye. Diffusion posterior sampling for general noisy inverse problems. In *The Eleventh International Conference on Learning Representations*, 2023.

Prafulla Dhariwal and Alexander Nichol. Diffusion models beat gans on image synthesis. *Advances in neural information processing systems*, 34:8780–8794, 2021.

Yilun Du and Leslie Pack Kaelbling. Position: Compositional generative modeling: A single model is not all you need. In *Forty-first International Conference on Machine Learning*, 2024.

Yilun Du, Shuang Li, and Igor Mordatch. Compositional visual generation with energy based models. *Advances in Neural Information Processing Systems*, 33:6637–6647, 2020.

Yilun Du, Conor Durkan, Robin Strudel, Joshua B Tenenbaum, Sander Dieleman, Rob Fergus, Jascha Sohl-Dickstein, Arnaud Doucet, and Will Sussman Grathwohl. Reduce, reuse, recycle: Compositional generation with energy-based diffusion models and mcmc. In *International conference on machine learning*, pp. 8489–8510. PMLR, 2023.

Patrick Esser, Sumith Kulal, Andreas Blattmann, Rahim Entezari, Jonas Müller, Harry Saini, Yam Levi, Dominik Lorenz, Axel Sauer, Frederic Boesel, et al. Scaling rectified flow transformers for high-resolution image synthesis. In *Forty-first International Conference on Machine Learning*, 2024.

Timur Garipov, Sebastiaan De Peuter, Ge Yang, Vikas Garg, Samuel Kaski, and Tommi Jaakkola. Compositional sculpting of iterative generative processes. *Advances in neural information processing systems*, 36:12665–12702, 2023.

Nico Giambi and Giuseppe Lisanti. Conditioning diffusion models via attributes and semantic masks for face generation. *arXiv preprint arXiv:2306.00914*, 2023.

Yuchao Gu, Xintao Wang, Jay Zhangjie Wu, Yujun Shi, Yunpeng Chen, Zihan Fan, Wuyou Xiao, Rui Zhao, Shuning Chang, Weijia Wu, et al. Mix-of-show: Decentralized low-rank adaptation for multi-concept customization of diffusion models. *Advances in Neural Information Processing Systems*, 36, 2024.

Yuwei Guo, Ceyuan Yang, Anyi Rao, Zhengyang Liang, Yaohui Wang, Yu Qiao, Maneesh Agrawala, Dahua Lin, and Bo Dai. Animatediff: Animate your personalized text-to-image diffusion models without specific tuning. In *The Twelfth International Conference on Learning Representations*, 2024.

Jiajun He, José Miguel Hernández-Lobato, Yuanqi Du, and Francisco Vargas. Rne: a plug-and-play framework for diffusion density estimation and inference-time control. *arXiv preprint arXiv:2506.05668*, 2025.

Amir Hertz, Andrey Voynov, Shlomi Fruchter, and Daniel Cohen-Or. Style aligned image generation via shared attention. In *Proceedings of the IEEE/CVF Conference on Computer Vision and Pattern Recognition*, pp. 4775–4785, 2024.

Jack Hessel, Ari Holtzman, Maxwell Forbes, Ronan Le Bras, and Yejin Choi. Clipscore: A reference-free evaluation metric for image captioning. In *Proceedings of the 2021 Conference on Empirical Methods in Natural Language Processing*, pp. 7514–7528, 2021.

Jonathan Ho, Ajay Jain, and Pieter Abbeel. Denoising diffusion probabilistic models. *Advances in neural information processing systems*, 33:6840–6851, 2020.

Jiun Tian Hoe, Xudong Jiang, Chee Seng Chan, Yap-Peng Tan, and Weipeng Hu. Interactdiffusion: Interaction control in text-to-image diffusion models. In *Proceedings of the IEEE/CVF Conference on Computer Vision and Pattern Recognition*, pp. 6180–6189, 2024.

Lianghua Huang, Di Chen, Yu Liu, Yujun Shen, Deli Zhao, and Jingren Zhou. Composer: creative and controllable image synthesis with composable conditions. In *Proceedings of the 40th International Conference on Machine Learning*, pp. 13753–13773, 2023a.

Nisha Huang, Yuxin Zhang, Fan Tang, Chongyang Ma, Haibin Huang, Weiming Dong, and Changsheng Xu. Diffstyler: Controllable dual diffusion for text-driven image stylization. *IEEE Transactions on Neural Networks and Learning Systems*, 2024.

Ziqi Huang, Tianxing Wu, Yuming Jiang, Kelvin CK Chan, and Ziwei Liu. Reversion: Diffusion-based relation inversion from images. *arXiv preprint arXiv:2303.13495*, 2023b.

Xu Jia, Takashi Isobe, Xiaomin Li, Qinghe Wang, Jing Mu, Dong Zhou, Huchuan Lu, Lu Tian, Ashish Sirasao, Emad Barsoum, et al. Customizing text-to-image generation with inverted interaction. In *ACM Multimedia 2024*, 2024.

Yuming Jiang, Tianxing Wu, Shuai Yang, Chenyang Si, Dahua Lin, Yu Qiao, Chen Change Loy, and Ziwei Liu. Videobooth: Diffusion-based video generation with image prompts. In *Proceedings of the IEEE/CVF Conference on Computer Vision and Pattern Recognition*, pp. 6689–6700, 2024.

Tero Karras, Miika Aittala, Timo Aila, and Samuli Laine. Elucidating the design space of diffusion-based generative models. *Advances in Neural Information Processing Systems*, 35:26565–26577, 2022.

Diederik P Kingma and Max Welling. Auto-encoding variational bayes. *arXiv preprint arXiv:1312.6114*, 2013.

Nupur Kumari, Bingliang Zhang, Richard Zhang, Eli Shechtman, and Jun-Yan Zhu. Multi-concept customization of text-to-image diffusion. In *Proceedings of the IEEE/CVF Conference on Computer Vision and Pattern Recognition*, pp. 1931–1941, 2023.

Tony Lee, Michihiro Yasunaga, Chenlin Meng, Yifan Mai, Joon Sung Park, Agrim Gupta, Yunzhi Zhang, Deepak Narayanan, Hannah Teufel, Marco Bellagente, et al. Holistic evaluation of text-to-image models. *Advances in Neural Information Processing Systems*, 36, 2024.

Dongxu Li, Junnan Li, and Steven Hoi. Blip-diffusion: Pre-trained subject representation for controllable text-to-image generation and editing. *Advances in Neural Information Processing Systems*, 36, 2024a.

Haoran Li, Haolin Shi, Wenli Zhang, Wenjun Wu, Yong Liao, Lin Wang, Lik-hang Lee, and Pengyuan Zhou. Dreamscene: 3d gaussian-based text-to-3d scene generation via formation pattern sampling. *arXiv preprint arXiv:2404.03575*, 2024b.

Yuheng Li, Haotian Liu, Qingyang Wu, Fangzhou Mu, Jianwei Yang, Jianfeng Gao, Chunyuan Li, and Yong Jae Lee. Gligen: Open-set grounded text-to-image generation. In *Proceedings of the IEEE/CVF Conference on Computer Vision and Pattern Recognition*, pp. 22511–22521, 2023.

Nan Liu, Shuang Li, Yilun Du, Antonio Torralba, and Joshua B Tenenbaum. Compositional visual generation with composable diffusion models. In *European Conference on Computer Vision*, pp. 423–439. Springer, 2022.

Shuailei Ma, Yuefeng Wang, Shanze Wang, and Ying Wei. Fgahoi: Fine-grained anchors for human-object interaction detection. *IEEE Transactions on Pattern Analysis and Machine Intelligence*, 2023.

Chong Mou, Xintao Wang, Jiechong Song, Ying Shan, and Jian Zhang. Diffeditor: Boosting accuracy and flexibility on diffusion-based image editing. In *Proceedings of the IEEE/CVF Conference on Computer Vision and Pattern Recognition*, pp. 8488–8497, 2024.

Alexander Quinn Nichol, Prafulla Dhariwal, Aditya Ramesh, Pranav Shyam, Pamela Mishkin, Bob McGrew, Ilya Sutskever, and Mark Chen. Glide: Towards photorealistic image generation and editing with text-guided diffusion models. In *International Conference on Machine Learning*, pp. 16784–16804. PMLR, 2022.

Weili Nie, Sifei Liu, Morteza Mardani, Chao Liu, Benjamin Eckart, and Arash Vahdat. Compositional text-to-image generation with dense blob representations. In *Forty-first International Conference on Machine Learning*, 2024.

Changdae Oh, Yixuan Li, Kyungwoo Song, Sangdoo Yun, and Dongyoon Han. Dawin: Training-free dynamic weight interpolation for robust adaptation. In *The Thirteenth International Conference on Learning Representations*, 2025.

Xu Peng, Junwei Zhu, Boyuan Jiang, Ying Tai, Donghao Luo, Jiangning Zhang, Wei Lin, Taisong Jin, Chengjie Wang, and Rongrong Ji. Portraitbooth: A versatile portrait model for fast identity-preserved personalization. In *Proceedings of the IEEE/CVF Conference on Computer Vision and Pattern Recognition*, pp. 27080–27090, 2024.

Dustin Podell, Zion English, Kyle Lacey, Andreas Blattmann, Tim Dockhorn, Jonas Müller, Joe Penna, and Robin Rombach. Sdxl: Improving latent diffusion models for high-resolution image synthesis. In *The Twelfth International Conference on Learning Representations*, 2024.

Tianhao Qi, Shancheng Fang, Yanze Wu, Hongtao Xie, Jiawei Liu, Lang Chen, Qian He, and Yong-dong Zhang. Deadiff: An efficient stylization diffusion model with disentangled representations. In *Proceedings of the IEEE/CVF Conference on Computer Vision and Pattern Recognition*, pp. 8693–8702, 2024.

Aditya Ramesh, Prafulla Dhariwal, Alex Nichol, Casey Chu, and Mark Chen. Hierarchical text-conditional image generation with clip latents. *arXiv preprint arXiv:2204.06125*, 1(2):3, 2022.

Robin Rombach, Andreas Blattmann, Dominik Lorenz, Patrick Esser, and Björn Ommer. High-resolution image synthesis with latent diffusion models. In *Proceedings of the IEEE/CVF conference on computer vision and pattern recognition*, pp. 10684–10695, 2022.

Simo Särkkä and Arno Solin. *Applied stochastic differential equations*, volume 10. Cambridge University Press, 2019.

Jing Shi, Wei Xiong, Zhe Lin, and Hyun Joon Jung. Instantbooth: Personalized text-to-image generation without test-time finetuning. In *Proceedings of the IEEE/CVF Conference on Computer Vision and Pattern Recognition*, pp. 8543–8552, 2024.

Marta Skretas, Tara Akhoun-Sadegh, Viktor Ohanesian, Roberto Bondesan, Alán Aspuru-Guzik, Arnaud Doucet, Rob Brekelmans, Alexander Tong, and Kirill Neklyudov. Feynman-kac correctors in diffusion: Annealing, guidance, and product of experts. *arXiv preprint arXiv:2503.02819*, 2025a.

Marta Skretas, Lazar Atanackovic, Joey Bose, Alexander Tong, and Kirill Neklyudov. The superposition of diffusion models using the itô density estimator. In *The Thirteenth International Conference on Learning Representations*, 2025b.

James Seale Smith, Yen-Chang Hsu, Lingyu Zhang, Ting Hua, Zsolt Kira, Yilin Shen, and Hongxia Jin. Continual diffusion: Continual customization of text-to-image diffusion with c-lora. *arXiv preprint arXiv:2304.06027*, 2023.

Jascha Sohl-Dickstein, Eric Weiss, Niru Maheswaranathan, and Surya Ganguli. Deep unsupervised learning using nonequilibrium thermodynamics. In *International conference on machine learning*, pp. 2256–2265. PMLR, 2015.

Kihyuk Sohn, Nataniel Ruiz, Kimin Lee, Daniel Castro Chin, Irina Blok, Huiwen Chang, Jarred Barber, Lu Jiang, Glenn Entis, Yuanzhen Li, et al. Styledrop: text-to-image generation in any style. In *Proceedings of the 37th International Conference on Neural Information Processing Systems*, pp. 66860–66889, 2023.

Jiaming Song, Chenlin Meng, and Stefano Ermon. Denoising diffusion implicit models. In *International Conference on Learning Representations*, 2021a.

Yang Song, Jascha Sohl-Dickstein, Diederik P Kingma, Abhishek Kumar, Stefano Ermon, and Ben Poole. Score-based generative modeling through stochastic differential equations. In *Proceedings of International Conference on Learning Representations (ICLR)*, 2021b.

James Thornton, Louis Béthune, Ruixiang Zhang, Arwen Bradley, Preetum Nakkiran, and Shuangfei Zhai. Composition and control with distilled energy diffusion models and sequential monte carlo. *arXiv preprint arXiv:2502.12786*, 2025.

Cong Wang, Kuan Tian, Yonghang Guan, Fei Shen, Zhiwei Jiang, Qing Gu, and Jun Zhang. Ensembling diffusion models via adaptive feature aggregation. In *The Thirteenth International Conference on Learning Representations*, 2025.

Ruichen Wang, Zekang Chen, Chen Chen, Jian Ma, Haonan Lu, and Xiaodong Lin. Compositional text-to-image synthesis with attention map control of diffusion models. In *Proceedings of the AAAI Conference on Artificial Intelligence*, volume 38, pp. 5544–5552, 2024a.

Xudong Wang, Trevor Darrell, Sai Saketh Rambhatla, Rohit Girdhar, and Ishan Misra. Instancediffusion: Instance-level control for image generation. In *Proceedings of the IEEE/CVF Conference on Computer Vision and Pattern Recognition*, pp. 6232–6242, 2024b.

Zhizhong Wang, Lei Zhao, and Wei Xing. Stylediffusion: Controllable disentangled style transfer via diffusion models. In *Proceedings of the IEEE/CVF International Conference on Computer Vision*, pp. 7677–7689, 2023.

Qiucheng Wu, Yujian Liu, Handong Zhao, Ajinkya Kale, Trung Bui, Tong Yu, Zhe Lin, Yang Zhang, and Shiyu Chang. Uncovering the disentanglement capability in text-to-image diffusion models. In *Proceedings of the IEEE/CVF conference on computer vision and pattern recognition*, pp. 1900–1910, 2023.

Guangxuan Xiao, Tianwei Yin, William T Freeman, Frédo Durand, and Song Han. Fastcomposer: Tuning-free multi-subject image generation with localized attention. *International Journal of Computer Vision*, pp. 1–20, 2024.

Jiazheng Xu, Xiao Liu, Yuchen Wu, Yuxuan Tong, Qinkai Li, Ming Ding, Jie Tang, and Yuxiao Dong. Imagereward: Learning and evaluating human preferences for text-to-image generation. *Advances in Neural Information Processing Systems*, 36, 2024.

Hu Ye, Jun Zhang, Sibo Liu, Xiao Han, and Wei Yang. Ip-adapter: Text compatible image prompt adapter for text-to-image diffusion models. *arXiv preprint arXiv:2308.06721*, 2023.

Yuxin Zhang, Nisha Huang, Fan Tang, Haibin Huang, Chongyang Ma, Weiming Dong, and Changsheng Xu. Inversion-based style transfer with diffusion models. In *Proceedings of the IEEE/CVF conference on computer vision and pattern recognition*, pp. 10146–10156, 2023.

Guangcong Zheng, Xianpan Zhou, Xuewei Li, Zhongang Qi, Ying Shan, and Xi Li. Layoutdiffusion: Controllable diffusion model for layout-to-image generation. In *Proceedings of the IEEE/CVF Conference on Computer Vision and Pattern Recognition*, pp. 22490–22499, 2023.

Dewei Zhou, You Li, Fan Ma, Xiaoting Zhang, and Yi Yang. Mige: Multi-instance generation controller for text-to-image synthesis. In *Proceedings of the IEEE/CVF Conference on Computer Vision and Pattern Recognition*, pp. 6818–6828, 2024.

A CONCENTRATION OF MEASURE THEOREM FOR HIGH-DIMENSIONAL INDEPENDENT NORMAL DISTRIBUTION

Lemma A.1. *Let $X = (X_1, X_2, \dots, X_n)$ be an n -dimensional random vector where each component X_i is independently and identically distributed as $\mathcal{N}(0, \sigma^2)$. Then, as the dimension n increases, the norm $\|X\|$ of X is concentrated around $\sqrt{n}\sigma$. Specifically, for any small $\epsilon \geq 0$ and sufficiently large n ,*

$$P(|\|X\| - \sqrt{n}\sigma| \leq \epsilon\sqrt{n}\sigma) \geq 1 - 2e^{-\frac{n\epsilon^2}{1+2\epsilon}} \quad (11)$$

This means X will concentrate near the hypersphere of radius $\sqrt{n}\sigma$ with high probability.

Proof: First, we consider the squared norm of a random vector X : $\|X\|^2 = X_1^2 + X_2^2 + \dots + X_n^2$. Since $X_i \sim \mathcal{N}(0, \sigma^2)$, it follows that $Y = \|X\|^2/\sigma^2 \sim \chi^2(n)$.

Using the Chernoff bound of the chi-square distribution:

$$P(Y \geq (1 + \delta)n) \leq e^{-\frac{n}{2}[\delta - \ln(1 + \delta)]}, \quad (12)$$

$$P(Y \leq (1 - \delta)n) \leq e^{-\frac{n}{2}[-\delta - \ln(1 - \delta)]}, \quad (13)$$

where $\delta \geq 0$ is a small value. According to $\ln(1 + \delta) \leq \frac{(2+\delta)\delta}{2(1+\delta)}$ and $\ln(1 - \delta) \leq -\delta - \frac{\delta^2}{2}$, we can deduce that:

$$\begin{aligned} P(\|X\|^2 \geq (1 + \delta)n\sigma^2) &= P(Y \geq (1 + \delta)n) \\ &\leq e^{-\frac{n\delta^2}{4(1+\delta)}} \end{aligned} \quad (14)$$

$$\begin{aligned} P(\|X\|^2 \leq (1 - \delta)n\sigma^2) &= P(Y \leq (1 - \delta)n) \\ &\leq e^{-\frac{n\delta^2}{4}} \\ &\leq e^{-\frac{n\delta^2}{4(1+\delta)}} \end{aligned} \quad (15)$$

Given the $\sqrt{1 + \delta} \leq 1 + \frac{\delta}{2}$ and $\sqrt{1 - \delta} \geq 1 - \frac{\delta}{2}$, we have:

$$\begin{aligned} P(\|X\| \geq (1 + \frac{\delta}{2})\sqrt{n}\sigma) &\leq P(\|X\| \geq \sqrt{(1 + \delta)}\sqrt{n}\sigma) \\ &\leq e^{-\frac{n\delta^2}{4(1+\delta)}} \end{aligned} \quad (16)$$

$$\begin{aligned} P(\|X\| \leq (1 - \frac{\delta}{2})\sqrt{n}\sigma) &\leq P(\|X\| \leq \sqrt{(1 - \delta)}\sqrt{n}\sigma) \\ &\leq e^{-\frac{n\delta^2}{4(1+\delta)}} \end{aligned} \quad (17)$$

Let $\epsilon = \delta/2$, and then organize equations (16) and (17):

$$P(|\|X\| - \sqrt{n}\sigma| \leq \epsilon\sqrt{n}\sigma) \geq 1 - 2e^{-\frac{n\epsilon^2}{1+2\epsilon}}, \quad (18)$$

which concludes the proof.

B PROOF OF PROPOSITION 3.1

Proposition 3.1. For the diffusion model p_{θ_1} defined by (6) and any new intermediate variable \mathbf{z}'_{t-1} from (8), let:

$$\tilde{\mathbf{z}}_{t-1} = \mathbf{z}'_{t-1} - \eta_{t-1}^{\theta_1} \frac{\mathbf{z}'_{t-1} - \mu_{\theta_1}(\mathbf{z}_t^{\theta_1}, t, y_1)}{\|\mathbf{z}'_{t-1} - \mu_{\theta_1}(\mathbf{z}_t^{\theta_1}, t, y_1)\|}, \quad (9)$$

where $\eta_{t-1}^{\theta_1}$ is a small optimization step size. There exists $\eta_{t-1}^{\theta_1}$ such that $\tilde{\mathbf{z}}_{t-1} \in D_{t-1, y_1}^{\theta_1}$. Moreover, an approximate lower bound on the probability that $\tilde{\mathbf{z}}_{t-1} \in D_{t-1, y_2}^{\theta_2}$ is given by:

$$P(\tilde{\mathbf{z}}_{t-1} \in D_{t-1, y_2}^{\theta_2}) \geq 1 - 2 \exp \left(-\frac{n \left(\epsilon_{t-1}^{\theta_2} - \frac{d}{\sigma_t \sqrt{n}} \right)^2}{1 + 2 \left(\epsilon_{t-1}^{\theta_2} - \frac{d}{\sigma_t \sqrt{n}} \right)} \right), \quad (10)$$

where $d = \phi_w(\varphi) \|\mathbf{z}_{t-1}^{\theta_1} - \mathbf{z}_{t-1}^{\theta_2}\| + \eta_{t-1}^{\theta_1}$ and $\phi_w(\varphi) = \sin((1-w)\varphi/2)/\sin(\varphi/2)$.

Proof:

(1) The existence of $\eta_{t-1}^{\theta_1}$ such that $\tilde{\mathbf{z}}_{t-1} \in D_{t-1, y_1}^{\theta_1}$:

We begin by defining the spherical shell as the high-probability set of $p_{\theta_i}(\mathbf{z}_{t-1}^{\theta_i} \mid \mathbf{z}_t^{\theta_i}, y_i)$

$$\mathcal{A}_{t-1, y_i}^{\theta_i}(\epsilon_{t-1}^{\theta_i}) = \left\{ \left| \|\mathbf{z}_{t-1}^{\theta_i} - \mu_{\theta_i}(\mathbf{z}_t^{\theta_i}, t, y_i)\| - \sqrt{n}\sigma_t \right| \leq \epsilon_{t-1}^{\theta_i} \sqrt{n}\sigma_t \right\}, \quad (19)$$

where $\epsilon_{t-1}^{\theta_i} = \sup \left\{ \epsilon \geq 0 : \mathcal{A}_{t-1, y_i}^{\theta_i}(\epsilon) \subseteq D_{t-1, y_i}^{\theta_i}(\tau_{t-1}^{\theta_i}) \right\}$.

Note that:

$$\begin{aligned} \nabla_{\mathbf{z}'_{t-1}} p_{\theta_1}(\mathbf{z}'_{t-1} \mid \mathbf{z}_t^{\theta_1}, y_1) &= \frac{1}{(2\pi\sigma_t^2)^{n/2}} \nabla_{\mathbf{z}'_{t-1}} \left(e^{-\frac{\|\mathbf{z}'_{t-1} - \mu_{\theta}(\mathbf{z}_t^{\theta_1}, t, y_1)\|^2}{2\sigma_t^2}} \right) \\ &= -\frac{1}{(2\pi\sigma_t^2)^{n/2}} e^{-\frac{\|\mathbf{z}'_{t-1} - \mu_{\theta}(\mathbf{z}_t^{\theta_1}, t, y_1)\|^2}{2\sigma_t^2}} \left(\frac{\mathbf{z}'_{t-1} - \mu_{\theta}(\mathbf{z}_t^{\theta_1}, t, y_1)}{\sigma_t^2} \right). \end{aligned} \quad (20)$$

Therefore,

$$\begin{aligned} \tilde{\mathbf{z}}_{t-1} &= \mathbf{z}'_{t-1} - \eta_{t-1}^{\theta_1} \frac{\mathbf{z}'_{t-1} - \mu_{\theta}(\mathbf{z}_t^{\theta_1}, t, y_1)}{\|\mathbf{z}'_{t-1} - \mu_{\theta}(\mathbf{z}_t^{\theta_1}, t, y_1)\|} \\ &= \mathbf{z}'_{t-1} + \eta_{t-1}^{\theta_1} \frac{\nabla_{\mathbf{z}'_{t-1}} p_{\theta_1}(\mathbf{z}'_{t-1} \mid \mathbf{z}_t^{\theta_1}, y_1)}{\|\nabla_{\mathbf{z}'_{t-1}} p_{\theta_1}(\mathbf{z}'_{t-1} \mid \mathbf{z}_t^{\theta_1}, y_1)\|}. \end{aligned} \quad (21)$$

This indicates that $\tilde{\mathbf{z}}_{t-1}$ is obtained from \mathbf{z}'_{t-1} by moving $\eta_{t-1}^{\theta_1}$ units in the radial direction opposite to $p_{\theta_1}(\mathbf{z}'_{t-1} \mid \mathbf{z}_t^{\theta_1}, y_1)$. Then, it suffices to ensure that:

$$\left| \|\mathbf{z}'_{t-1} - \mu_{\theta}(\mathbf{z}_t^{\theta_1}, t, y_1)\| + \eta_{t-1}^{\theta_1} - \sqrt{n}\sigma_t \right| < \epsilon_{t-1}^{\theta_1} \sqrt{n}\sigma_t, \quad (22)$$

from which we obtain:

$$-\epsilon_{t-1}^{\theta_1} \sqrt{n}\sigma_t - \|\mathbf{z}'_{t-1} - \mu_{\theta}(\mathbf{z}_t^{\theta_1}, t, y_1)\| + \sqrt{n}\sigma_t < \eta_{t-1}^{\theta_1} < \epsilon_{t-1}^{\theta_1} \sqrt{n}\sigma_t - \|\mathbf{z}'_{t-1} - \mu_{\theta}(\mathbf{z}_t^{\theta_1}, t, y_1)\| + \sqrt{n}\sigma_t, \quad (23)$$

thus, we have $\tilde{\mathbf{z}}_{t-1} \in \mathcal{A}_{t-1, y_1}^{\theta_1} \subseteq D_{t-1, y_1}^{\theta_1}$, which completes the proof of existence.

(2) The approximate lower bound on the probability that $\tilde{\mathbf{z}}_{t-1} \in D_{t-1, y_2}^{\theta_2}$:

By the triangle inequality, for any $z_{t-1}^{\theta_2} \in \mathcal{A}_{t-1, y_2}^{\theta_2}$, we have:

$$\|\tilde{\mathbf{z}}_{t-1} - \mathbf{z}_{t-1}^{\theta_2}\| \leq \|\mathbf{z}'_{t-1} - \mathbf{z}_{t-1}^{\theta_2}\| + \eta_{t-1}^{\theta_1}. \quad (24)$$

Since \mathcal{M}_{t-1} approximates an n -dimensional hypersphere as t becomes large, we may assume that $\|\mathbf{z}_{t-1}^{\theta_1}\| \approx \|\mathbf{z}_{t-1}^{\theta_2}\| \approx r_{t-1}$. For the validity of this assumption, please refer to the analysis in the Appendix C.2. Let φ be the angle between $\mathbf{z}_{t-1}^{\theta_1}$ and $\mathbf{z}_{t-1}^{\theta_2}$, then, the chord lengths satisfy:

$$\|\mathbf{z}'_{t-1} - \mathbf{z}_{t-1}^{\theta_2}\| = 2r_t \sin\left(\frac{(1-w)\varphi}{2}\right), \quad \delta = \|\mathbf{z}_{t-1}^{\theta_1} - \mathbf{z}_{t-1}^{\theta_2}\| = 2r_t \sin\left(\frac{\varphi}{2}\right).$$

Dividing the two identities yields:

$$\|\mathbf{z}'_{t-1} - \mathbf{z}_{t-1}^{\theta_2}\| = \phi_w(\varphi) \delta, \quad \phi_w(\varphi) = \frac{\sin\left(\frac{(1-w)\varphi}{2}\right)}{\sin\left(\frac{\varphi}{2}\right)}. \quad (25)$$

Combining (24) and (25), denote $d = \phi_w(\varphi) \delta + \eta_{t-1}^{\theta_1}$ and We can obtain the bound:

$$\text{dist}(\tilde{\mathbf{z}}_{t-1}, \mathcal{A}_{t-1, y_2}^{\theta_2}) \leq d. \quad (26)$$

So, we can also refer to d as the maximum distance to Model 2. This implies that, if:

$$|\|\mathbf{z}_{t-1}^{\theta_2} - \mu_{\theta_2}\| - \sigma_t \sqrt{n}| \leq (\epsilon_{t-1}^{\theta_2} - d/\sigma_t \sqrt{n}) \sigma_t \sqrt{n}, \quad (27)$$

then $B(\mathbf{z}_{t-1}^{\theta_2}, d) \subseteq \mathcal{A}_{t-1, y_2}^{\theta_2}$. Therefore:

$$\begin{aligned} P(\tilde{\mathbf{z}}_{t-1} \in D_{t-1, y_2}^{\theta_2}) &\geq P(\tilde{\mathbf{z}}_{t-1} \in \mathcal{A}_{t-1, y_2}^{\theta_2}) \\ &\geq P(|\|\mathbf{z}_{t-1}^{\theta_2} - \mu_{\theta_2}\| - \sigma_t \sqrt{n}| \leq (\epsilon_{t-1}^{\theta_2} - \frac{d}{\sigma_t \sqrt{n}}) \sigma_t \sqrt{n}) \\ &\geq 1 - 2 \exp\left(-\frac{n \left(\epsilon_{t-1}^{\theta_2} - \frac{d}{\sigma_t \sqrt{n}}\right)^2}{1 + 2 \left(\epsilon_{t-1}^{\theta_2} - \frac{d}{\sigma_t \sqrt{n}}\right)}\right). \end{aligned} \quad (28)$$

The first line follows from $\tilde{\mathbf{z}}_{t-1} \in \mathcal{A}_{t-1, y_2}^{\theta_2} \subseteq D_{t-1, y_2}^{\theta_2}$, and the third line follows from Lemma A.1, which concludes the proof.

C STATISTICAL ANALYSIS

C.1 GAUSSIANITY IN LATENT SPACE

Chung et al. (2022) has shown that \mathcal{M}_t is concentrated on an $(n-1)$ -dimensional manifold, which approximates an n -dimensional hypersphere as t becomes large. Motivated by this property, in order to reduce manifold deviation, the AMDM algorithm performs spherical aggregation during the initial s steps of inference when t is large. Next, we focus on the statistical characteristics of the distribution $p(\mathbf{z}_t)$, in particular its first and second-order moments, to validate the appropriateness of the hyperspherical approximation in the large t regime. This analysis further reinforces the motivation for applying spherical aggregation during the initial stages of inference in AMDM.

The continuous form of (1) can be rewrite as:

$$d\mathbf{z}_t = -\frac{1}{2} g_t^2 \mathbf{z}_t dt + g_t d\mathbf{w}_t, \quad (29)$$

We can use equations (5.50) and (5.51) (Särkkä & Solin, 2019) to derive the relationship between the mean and variance of (29) as they evolve over time:

$$\frac{d\mathbf{m}}{dt} = \mathbb{E}\left[-\frac{1}{2} g_t^2 \mathbf{z}_t\right] = -\frac{1}{2} g_t^2 \mathbf{m} \quad (30)$$

$$\begin{aligned} \frac{d\mathbf{P}}{dt} &= \mathbb{E}\left[-\frac{1}{2} g_t^2 \mathbf{z}_t (\mathbf{z}_t)^T\right] + \mathbb{E}\left[-\frac{1}{2} g_t^2 (\mathbf{z}_t - \mathbf{m}) \mathbf{z}_t^T\right] + g_t^2 \mathbf{I} \\ &= -g_t^2 \mathbf{P} + g_t^2 \mathbf{I} \end{aligned} \quad (31)$$

The solutions are:

$$\mathbf{m}(t) = \mathbf{m}(0) e^{-\frac{1}{2} \int_0^t g_s^2 ds} \quad (32)$$

$$\mathbf{P}(t) = \mathbf{I} + (\mathbf{P}(0) - \mathbf{I}) e^{-\int_0^t g_s^2 ds}, \quad (33)$$

where $g_t = \sqrt{\beta_t}$, and we set β_t to follow the linear schedule in SD (Rombach et al., 2022). For $\mathbf{m}(0)$ and $\mathbf{P}(0)$, since the data $\mathbf{z}_0^{(i)} \in [-1, 1]$, it follows that $\mathbf{m}(0)^{(i)} \in [-1, 1]$ and $\mathbf{P}(0)^{(i)} \in [0, 1]$. Therefore, we consider the extreme case with $\mathbf{m}(0) = \mathbf{I}$ and $\mathbf{P}(0) = \mathbf{0}$. The resulting mean and variance of $p(\mathbf{z}_t)$ as functions of time are shown in the Figure 6.

From the Figure 6, it can be observed that when $t > 0.6$, the mean rapidly converges to 0 while the variance rapidly converges to 1, approaching a standard Gaussian distribution. This indicates the rationality of proposing the spherical aggregation operation during the first s steps in the AMDM algorithm experiments.

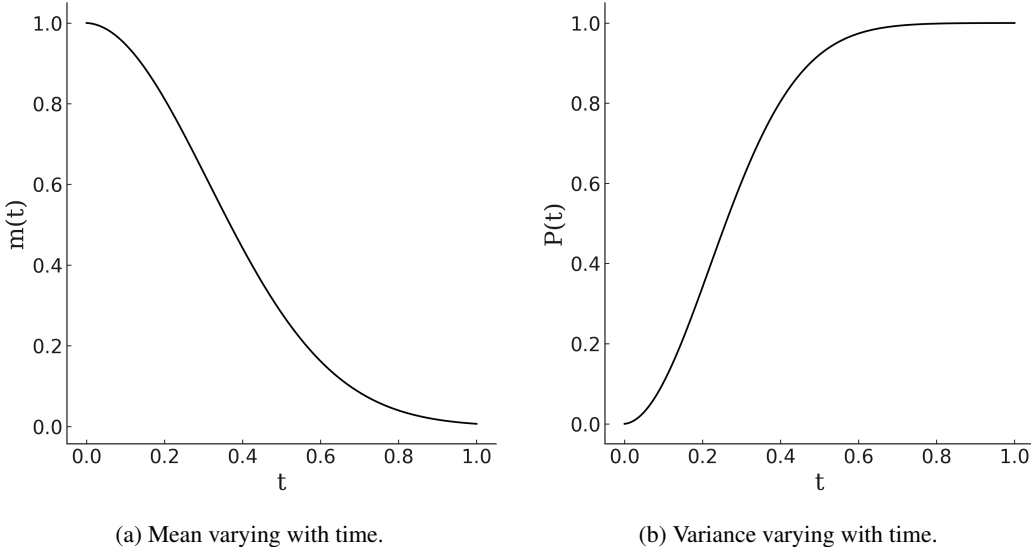


Figure 6: Statistical properties of $p(\mathbf{z}_t)$ over time.

C.2 ASSUMPTION OF EQUAL MAGNITUDES

In the proof of Proposition 3.1, we assume during aggregation that $\|\mathbf{z}_t^{\theta_1}\| \approx \|\mathbf{z}_t^{\theta_2}\| \approx r_t$. To assess the plausibility of this assumption, we log intermediate variables from InteractDiffusion(+MIGC) and report them in Table 5 and Figure 7. During the first $s = 20$ aggregation steps ($t = 50$ to $t = 30$), $\|\mathbf{z}_t^{\theta_1}\| - \|\mathbf{z}_t^{\theta_2}\| \approx 0$, which directly supports the equal-norm assumption. This behavior is expected for the following reasons. At initialization ($t = 50$), both trajectories are sampled from the standard Gaussian and thus have numerically almost identical magnitudes; the subsequent single-step denoising from $t = 50 \rightarrow 49$, although performed by different models, introduces only a small variations, so the magnitudes remain nearly equal. Moreover, the small variations in the angle φ and in the difference norm $\|\mathbf{z}_t^{\theta_1} - \mathbf{z}_t^{\theta_2}\|$ further indicate that the per-step generative error is well controlled. Once aggregation takes effect, $\mathbf{z}_{t-1}^{\theta_1}$ and $\mathbf{z}_{t-1}^{\theta_2}$ start from the common aggregation point \mathbf{z}'_t , undergo small deviation optimization, and are then sampled separately; because the aggregation point is shared, the deviations are limited, and each sampling step introduces only a small error, the magnitudes remain almost equal. Taken together, these observations justify the equal-norm assumption throughout the aggregation process.

C.3 MAXIMUM DISTANCE TERM

In Proposition 3.1, we derived the approximate lower bound of the probability:

$$P\left(\tilde{\mathbf{z}}_{t-1} \in D_{t-1, y_2}^{\theta_2}\right) \geq 1 - 2 \exp\left(-\frac{n\left(\epsilon_{t-1}^{\theta_2} - \frac{d}{\sigma_t \sqrt{n}}\right)^2}{1 + 2\left(\epsilon_{t-1}^{\theta_2} - \frac{d}{\sigma_t \sqrt{n}}\right)}\right), \quad (10)$$

where the key quantity is the maximum distance to the model, given by $d = \phi_w(\varphi) \delta + \eta_{t-1}^{\theta_1}$. The numerical value of d directly determines whether the optimized variable $\mathbf{z}_t^{\theta_1}$ is likely to lie on the data manifold of model θ_2 , thereby enabling fine-grained generation. Theoretically, the smaller the value of d , the higher the likelihood. To this end, we separately analyze $\phi_w(\varphi) = \frac{\sin((1-w)\varphi/2)}{\sin(\varphi/2)}$ and $\delta = \|\mathbf{z}_{t-1}^{\theta_1} - \mathbf{z}_{t-1}^{\theta_2}\|$.

For $\phi_w(\varphi)$, we first examine the variation of the angle φ over time. The detailed experimental results can be referred to in the Table 5 and Fig 8a. At the initial step $t = 50$, since random points

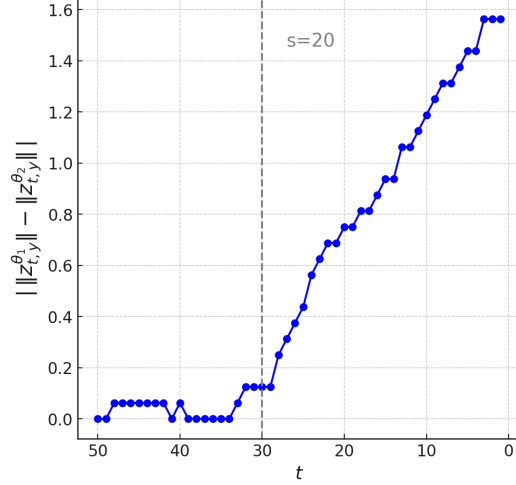


Figure 7: Difference of norm varying with time.

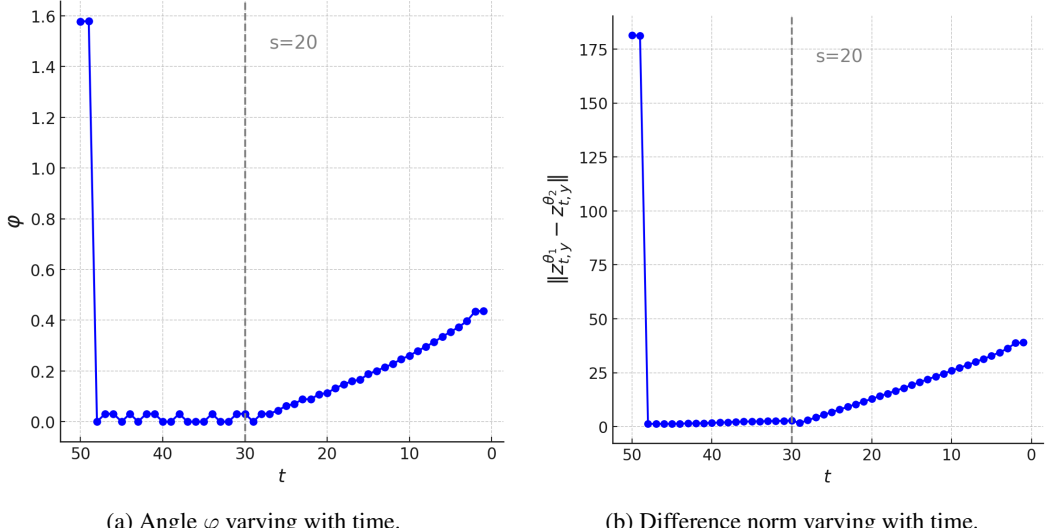


Figure 8: Variation of the Angle and the Difference Norm.

in high-dimensional Gaussian space are almost orthogonal, the angle satisfies $\varphi \approx \frac{\pi}{2}$. At $t = 49$, a single sampling step of the model introduces only a negligible perturbation, so φ remains essentially unchanged. Subsequently, following an argument similar to the analysis of difference of norm in Appendix C.2: since $\mathbf{z}_{t-1}^{\theta_1}$ and $\mathbf{z}_{t-1}^{\theta_2}$ are both derived from the common aggregation point \mathbf{z}'_t , and then undergo deviation optimization and independent sampling, these operations only introduce small perturbations, implying that φ also stays small. Expanding $\phi_w(\varphi)$ in a Taylor series gives $\phi_w(\varphi) = (1 - w) + O(\varphi^2)$. Since φ is very small, the higher-order terms can be neglected, yielding $\phi_w(\varphi) \approx (1 - w)$. In summary, at the initial step, $\phi_w(\varphi) \approx \phi_w(\frac{\pi}{2}) = \sqrt{2} \sin\left(\frac{(1-w)\pi}{4}\right) \leq 1$, whereas after aggregation, $\phi_w(\varphi) \approx (1 - w) \leq 1$. Thus, we conclude that $\phi_w(\varphi) \leq 1$.

For δ , the specific experimental values are provided in the Table 5 and Figure 8b. Based on a similar analysis as above, it can be inferred that at the initial steps $t = 50$ and $t = 49$, the vectors are generated by random sampling, leading to a large magnitude of their difference. In subsequent steps, however, since both vectors originate from the same aggregation point of the previous step

t	φ	$\ \mathbf{z}_t^{\theta_1} - \mathbf{z}_t^{\theta_2}\ $	$\ \mathbf{z}_t^{\theta_1}\ - \ \mathbf{z}_t^{\theta_2}\ $
50	1.5781	181.3750	0.0000
49	1.5791	181.2500	0.0000
48	0.0000	1.3086	0.0625
47	0.0312	1.3125	0.0625
46	0.0312	1.3281	0.0625
45	0.0000	1.3652	0.0625
44	0.0312	1.4219	0.0625
43	0.0000	1.5244	0.0625
42	0.0312	1.5625	0.0625
41	0.0312	1.6426	0.0000
40	0.0000	1.7812	0.0625
39	0.0000	1.8926	0.0000
38	0.0312	2.0586	0.0000
37	0.0000	2.2402	0.0000
36	0.0000	2.3730	0.0000
35	0.0000	2.4258	0.0000
34	0.0312	2.4707	0.0000
33	0.0000	2.5508	0.0625
32	0.0000	2.6309	0.1250
31	0.0312	2.7324	0.1250
30	0.0312	2.8184	0.1250
29	0.0000	1.6904	0.1250
28	0.0312	2.9727	0.2500
27	0.0312	4.2734	0.3125
26	0.0442	5.5273	0.3750
25	0.0625	6.7500	0.4375
24	0.0699	7.9648	0.5625
23	0.0884	9.1797	0.6250
22	0.0884	10.4141	0.6875
21	0.1083	11.6406	0.6875
20	0.1127	12.8750	0.7500
19	0.1327	14.1250	0.7500
18	0.1467	15.3750	0.8125
17	0.1595	16.6406	0.8125
16	0.1655	17.9219	0.8750
15	0.1877	19.2500	0.9375
14	0.2004	20.5938	0.9375
13	0.2146	21.9219	1.0625
12	0.2280	23.2500	1.0625
11	0.2467	24.5781	1.1250
10	0.2603	25.9219	1.1875
9	0.2786	27.2656	1.2500
8	0.2959	28.6094	1.3125
7	0.3137	29.9844	1.3125
6	0.3352	31.3906	1.3750
5	0.3540	32.8438	1.4375
4	0.3733	34.4062	1.4375
3	0.3967	36.1875	1.5625
2	0.4353	38.8125	1.5625
1	0.4365	38.9688	1.5625

Table 5: Values of different intermediate variables over time in InteractDiffusion (+MIGC)

and the following operations introduce only small perturbations, the magnitude of their difference becomes significantly smaller.

In summary, only after the first aggregation optimization may the variable $\tilde{\mathbf{z}}_{T-1}$ deviate from $D_{T-1, y_2}^{\theta_2}$. In the subsequent aggregation steps, however, $\tilde{\mathbf{z}}_{t, y_2}$ remains, with high probability, within $D_{t, y_2}^{\theta_2}$, thereby fully incorporating the characteristics of different models and enabling fine-grained generation. This observation is also intuitive: since the initial sampling is performed from two ran-

dom points that are relatively far apart, it is difficult for the first aggregation to lie simultaneously on the manifolds of both models at step $T - 1$.

In addition, we conducted 10 additional tests with different random seeds. The results show that the angle φ and the difference of norm $\|\mathbf{z}_t^{\theta_1}\| - \|\mathbf{z}_t^{\theta_2}\|$ remain nearly identical across experiments, while the difference norm $\|\mathbf{z}_{t-1}^{\theta_1} - \mathbf{z}_{t-1}^{\theta_2}\|$ fluctuates only within ± 1 . Hence, the above analysis can be regarded as robust.

D EXPERIMENTAL DETAILS

D.1 EVALUATION METRICS

COCO-MIG Benchmark (Zhou et al., 2024) assess the enhancement in attribute metrics. The COCO-MIG Benchmark is based on the COCO-position layout, where each instance is assigned a color attribute, requiring the generated instances to satisfy both position and color constraints. The process includes sampling layouts from COCO and categorizing layouts into five levels (L2-L6) based on the number of instances. Then, colors are assigned to each instance, global prompts are constructed, and a test file containing 800 entries is generated. The COCO-MIG metrics primarily include Instance Success Rate and mIoU Score. The Instance Success Rate measures the probability of each instance being generated correctly, while mIoU Score calculates the average of the maximum IoU for all instances; if the color attribute is incorrect, the IoU value is set to 0. Since the MIG-Benchmark does not contain interactive prompt, we set the "action" input in the InteractDiffusion model to "and".

FGAHOI (Ma et al., 2023) can measure interaction controllability. We use the FGAHOI model based on the Swin-Tiny architecture, as an HOI detector to evaluate the model's ability to control interactions. HOI Detection Scores are categorized into two types: Default and Known Object. The Default setting is more challenging, as it requires distinguishing between irrelevant images.

CLIP (Hessel et al., 2021) is the CLIPScore of the generated images with captions of the image prompts.

D.2 PARAMETER SETTINGS

InteractDiffusion and MIGC. The total sampling steps T are set to 50, the aggregation step s is set to 20, the weighting factor w is set to 0.5 and the optimization steps $\eta_t^{\theta_1}$ and $\eta_t^{\theta_2}$ are both set to 0.3. We use InteractDiffusion v1.0, and MIGC is modified to use the DDIM sampling method to align with the same diffusion process.

InteractDiffusion and IP-Adapter. The total sampling steps T are set to 10, the aggregation step s is set to 5, the weighting factor w is set to 0.5, ip scale is set to 0.8 and the optimization steps $\eta_t^{\theta_1}$ and $\eta_t^{\theta_3}$ are both set to 0.3. We utilized IP-Adapter based on SD1.5 while keeping InteractDiffusion unchanged.

InteractDiffusion, MIGC and IP-Adapter. The pretrained models for the three architectures remain consistent with those mentioned above. The total sampling step T set to 10, an aggregation step s set to 5, and weight factors w_1 and w_2 set to 0.5 and 0.65. The optimization steps $\eta_t^{\theta_1}$, $\eta_t^{\theta_2}$, and $\eta_t^{\theta_3}$ are all simply set to 0.3, respectively.

D.3 ADDITIONAL EXPERIMENTS

In order to further evaluate the style feature, we additionally provide CLIP scores also on COCO validation set for reference. Table 6 shows a significant improvement in the aggregated style control from 0.533 to 0.581, nearly reaching the performance of IP-Adapter, also demonstrating the effectiveness of AMDM.

In the main experiments, we have used different diffusion versions to validate the generality: the IP-Adapter model is based on SD1.5, while InteractDiffusion and MIGC are based on SD1.4. Additionally, we conducted further experiments using SDXL-based InteractDiffusion and IP-Adapter.

Method	CLIP \uparrow
InteractDiffusion	0.533
InteractDiffusion(+IP-Adapter)	0.581
IP-Adapter	0.588

Table 6: CLIP scores for InteractDiffusion(+IP-Adapter).

SDXL and SD 1.4/1.5 use different noise schedulers, i.e., their corresponding SDEs are inconsistent. We also used CLIP to evaluate style features. As shown in the Table 7, the style control significantly improves from 0.545 to 0.597, nearly reaching the performance of IP-Adapter. Because AMDM operates exclusively on the intermediate latent variables \mathbf{z}_t of the diffusion process rather than on the parameterization of noise prediction, it is intrinsically decoupled from both ϵ -prediction and v -prediction. Consequently, as long as the latent \mathbf{z}_t at the same time step t is accessible, the method can be seamlessly paired with different prediction parameterizations and samplers without modifying model weights or training objectives, demonstrating broad applicability and portability.

Method	CLIP \uparrow
InteractDiffusion	0.545
InteractDiffusion(+IP-Adapter)	0.597
IP-Adapter	0.613

Table 7: CLIP scores for InteractDiffusion(+IP-Adapter) based on SDXL.

Finally, we conduct experiments using InteractDiffusion based on SD1.4 and MIGC based on EDM sampling. As shown in Table 8, when the two models are not derived from the same SDE, the AMDM algorithm fails: the generated images exhibit poor quality and deviate from the data manifold, since the two data domains do not lie on the same \mathcal{M}_t , making aggregation inapplicable. The fundamental requirement of AMDM is a shared encoder and diffusion SDE, while no constraint is imposed on the denoising network. Considering that many recent works build upon the same pretrained models for secondary development, these requirements are relatively easy to satisfy in practice, granting AMDM broad applicability. In contrast, works such as (Biggs et al., 2024; Oh et al., 2025; Wang et al., 2025) impose an additional restriction, requiring identical denoising networks. From this perspective, AMDM supports a wider range of application scenarios.

Table 8: Quantitative results on the COCO-MIG benchmark and CLIP Score in InteractDiffusion(+MIGC).

Method	Instance Success Rate (%) \uparrow						mIoU Score (%) \uparrow						CLIP Score \uparrow	
	L_2	L_3	L_4	L_5	L_6	Avg	L_2	L_3	L_4	L_5	L_6	Avg	Global	Local
InteractDiffusion	37.50	35.62	35.31	30.62	34.16	34.06	32.98	31.63	30.82	28.29	30.40	30.40	31.09	27.56
InteractDiffusion(+MIGC)	20.03	18.67	18.45	15.62	16.29	18.13	17.64	16.38	15.60	13.25	14.98	15.03	14.77	13.91
MIGC	67.70	59.61	58.09	56.16	56.88	58.43	59.39	52.73	51.45	49.52	49.89	51.48	33.01	28.95

E COMPARISON WITH COMPOSITIONAL METHODS

Compositional generation aims to synthesize complex new samples that simultaneously satisfy multiple attributes or concepts by combining information from multiple different distributions. In the context of diffusion models, this is often achieved by combining the score functions $\nabla_x \log p_t(x)$ of the noise processes from different models to simulate a new reverse stochastic differential equation (SDE).

Du et al. (2023) proposed an energy-based framework for compositional generation, where the scores from multiple models are summed to approximate the score of the joint distribution, that is:

$$\nabla \log p_{\text{PoE}}(x) \approx \sum_{i=1}^N \nabla \log p_i(x),$$

and the corresponding target distribution is the Product of Experts (PoE):

$$p_{\text{PoE}}(x) \propto \prod_{i=1}^N p_i(x).$$

Sampling is performed using MCMC methods such as Langevin dynamics or HMC. However, these approaches are heuristic in nature, lack theoretical guarantees, and incur high computational costs.

Skreta et al. (2025a) introduce the *Feynman-Kac Corrector (FKC)* framework, which provides a principled approach to sampling from modified target distributions:

$$\begin{aligned} \textbf{Annealed: } \quad p_{t,\beta}^{\text{anneal}}(x) &= \frac{1}{Z_t(\beta)} q_t(x)^\beta, \\ \textbf{Product: } \quad p_t^{\text{prod}}(x) &= \frac{1}{Z_t} q_t^1(x) q_t^2(x), \\ \textbf{Geometric Avg: } \quad p_{t,\beta}^{\text{geo}}(x) &= \frac{1}{Z_t(\beta)} q_t^1(x)^{1-\beta} q_t^2(x)^\beta. \end{aligned}$$

They derive weighted SDEs:

$$dx_t = (-f_t(x_t) + \sigma_t^2 \nabla \log p_t(x_t)) dt + \sigma_t dW_t,$$

and apply Sequential Monte Carlo (SMC) to correct sample trajectories. This framework generalizes classifier-free guidance (CFG) and improves inference-time controllability.

Thornton et al. (2025) introduce a novel framework that distills pretrained diffusion models into energy-parameterized models, where the score function is expressed as the gradient of a learned energy $s(x, t) = -\nabla_x E_\theta(x, t)$. To address training instability common in energy-based models, they propose a conservative projection loss that distills the score function from a pretrained teacher model:

$$\min_{\theta} \mathbb{E}_{p_t} [\|\nabla E_\theta(x, t) + s_{\text{teacher}}(x, t)\|^2].$$

This energy formulation enables the definition of new target distributions for sampling. Specifically, in compositional generation tasks, they define a composed distribution as the product of multiple submodels:

$$p(x) \propto \prod_i \exp(-E_i(x)) = \exp\left(-\sum_i E_i(x)\right),$$

which implies that the composed score is equivalent to the sum of individual scores:

$$\nabla \log p(x) = -\sum_i \nabla E_i(x) = \sum_i s_i(x).$$

This resembles the linear score composition used in prior works such as projective composition, but, unlike those methods, which plug the summed scores directly into the reverse diffusion equation.

Bradley et al. (2025) provide a theoretical foundation for *projective composition*. Assuming a *Factorized Conditional* structure, they show:

$$\nabla \log p(x) = \sum_i \nabla_x \log p_i(x) - (k-1) \nabla_x \log p_b(x).$$

where $p_b(x)$ is the background distribution (as in the unconditional model). This combination corresponds to a Bayesian fusion distribution:

$$p(x) \propto \frac{\prod_i p_i(x)}{p_b(x)^{k-1}}.$$

This enables direct reverse diffusion sampling without correction under appropriate assumptions. Furthermore, they generalize to feature space combinations, where orthogonal transformations $z = A(x)$ can preserve compositionality.

Skreta et al. (2025b) leverage the Itô density estimator to dynamically weight the score functions of different models, yielding a new generative vector field. Given M diffusion models with score functions $\nabla \log q_t^i(x)$, SUPERDIFF defines:

$$u_\tau(x) = \sum_{i=1}^M \kappa_\tau^i(x) \nabla \log q_t^i(x).$$

In the OR mode (mixture of densities), the weights are defined by a softmax over the estimated log-densities:

$$\kappa_\tau^i(x) = \frac{\exp(T \cdot \log q_t^i(x) + \ell)}{\sum_j \exp(T \cdot \log q_t^j(x) + \ell)},$$

allowing the combined model to generate samples consistent with any of the component models. In the AND mode (intersection of densities), the weights are obtained by solving a linear system such that all log-densities evolve consistently:

$$\sum_{i=1}^M \kappa_\tau^i(x) \frac{d}{d\tau} \log q_t^i(x) \approx \text{constant across } i,$$

enforcing agreement among models and producing samples that satisfy all constraints simultaneously. Finally, the sampling process follows the reverse-time SDE:

$$dx_\tau = (-f_{1-\tau}(x_\tau) + g_{1-\tau}^2 u_\tau(x_\tau)) d\tau + g_{1-\tau} dW_\tau,$$

which yields samples representing either the union (OR) or the intersection (AND) of the underlying model distributions.

To further compare the differences in task adaptation, we also provide compositional methods with the same fine-grained input and conduct compositional experiments on both MIGC and InteractDiffusion. The results are compared with the AMDM method and presented in Table 9.

Table 9: Composition of MIGC and InteractDiffusion on the COCO-MIG Benchmark

Method	Instance Success Rate Avg \uparrow	mIoU Score Avg \uparrow	Time (s) \downarrow
Du et al. (2023)	51.29	41.22	42.6
Bradley et al. (2025)	32.74	28.65	12.9
Skreta et al. (2025a)	30.21	27.49	11.3
Skreta et al. (2025b)	52.53	45.21	14.3
AMDM	54.78	47.74	8.8 (single model 7.5s)

From equation (4), we observe that the linear combination of different \mathbf{z}_t from various models corresponds to the linear combination of their predicted noise, which is proportional to the score. Therefore, the linear combination in AMDM can be interpreted as a linear combination of scores, which is actually similar to the compositional methods. As shown in our aggregation ablation study of AMDM in Figure 5b, linear combination performs worse than spherical aggregation. This is because, in fine-grained generation, the data lies on a spherical manifold, and spherical aggregation better preserves generation quality. Although Du’s method (Du et al., 2023) applies Langevin dynamics to improve sample quality after linear aggregation and achieves good results, it comes with substantial computational overhead. Similarly, SUPERDIFF (Skreta et al., 2025b) reduces manifold deviation from a methodological perspective and achieves favorable performance. However, in fine-grained generation scenarios, its “AND” mode requires solving a system of linear equations, which introduces additional overhead. Moreover, Bradley’s work (Bradley et al., 2025) theoretically proves that linear score combination only yields high-quality results when the compositional conditions lie in orthogonal feature spaces. However, fine-grained generation typically involves nearly identical conditions, which clearly violates this assumption, providing theoretical support for the observed experimental results.

Finally, we conduct a simple compositional generation experiment (2D Composition Mixture) to illustrate the limitations of AMDM in compositional generation. The experimental results are shown in Table 10. The reason for the failure of the AMDM algorithm is also quite simple: AMDM is only

applicable under the approximate high-dimensional Gaussian distribution; for general distributions, spherical aggregation and deviation optimization fail. It is clear that AMDM differs significantly from other combination methods in terms of application scenarios.

Table 10: Comparison of AMDM and Du 2023 under a non-Gaussian distribution

Method	ln(MMD) ↓	LL ↑	Var ↓
AMDM	-3.51	-2.43	0.032
Du et al. (2023)	-4.48	1.30	0.007

F LIMITATIONS AND BROAD IMPACTS

We propose a novel aggregation algorithm AMDM. This algorithm is specifically designed for fine-grained generation tasks using conditional diffusion models, under the constraint encoders and diffusion process, independent of denoising network structure. At present, the selection of the hyperparameter η in the AMDM algorithm is largely heuristic. In future work, we will investigate dynamic adaptive selection strategies that are grounded in data-driven criteria or theoretical analysis to enhance the model’s robustness and generalization. As demonstrated in the experiments in Appendix E, AMDM is different from previous composition-based generation methods and is tailored for fine-grained generation. Furthermore, we advocate against injecting harmful features into high-quality models to prevent the generation of socially harmful images.

G ADDITIONAL VISUAL RESULTS

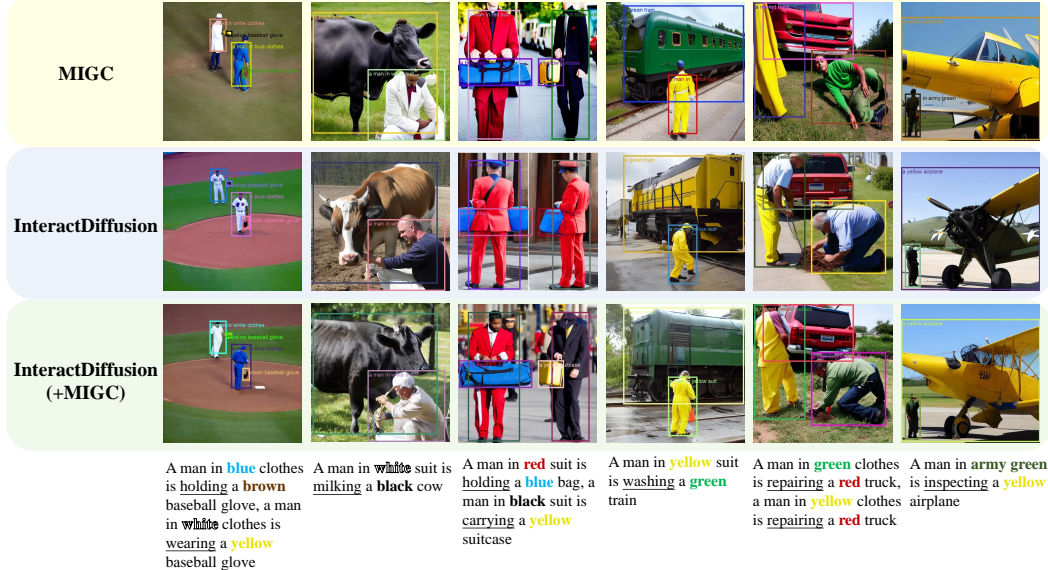


Figure 9: Additional Visual results of aggregating MIGC into InteractDiffusion applying the AMDM algorithm.

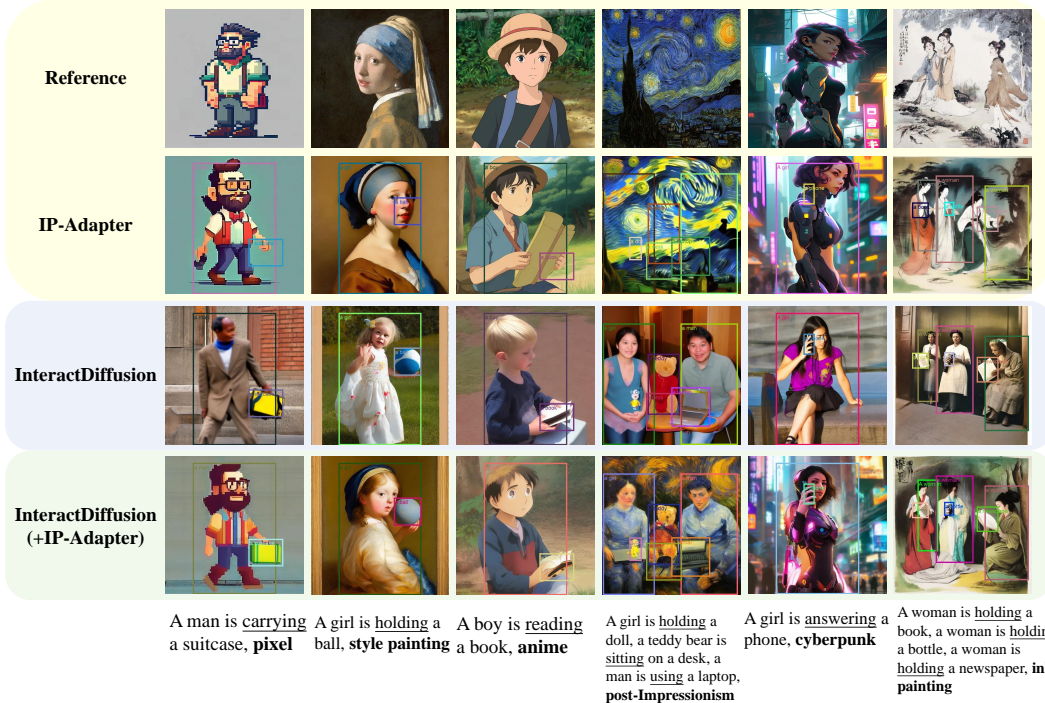


Figure 10: Additional Visual results of aggregating IP-Adapter into InteractDiffusion applying AMDM algorithm.

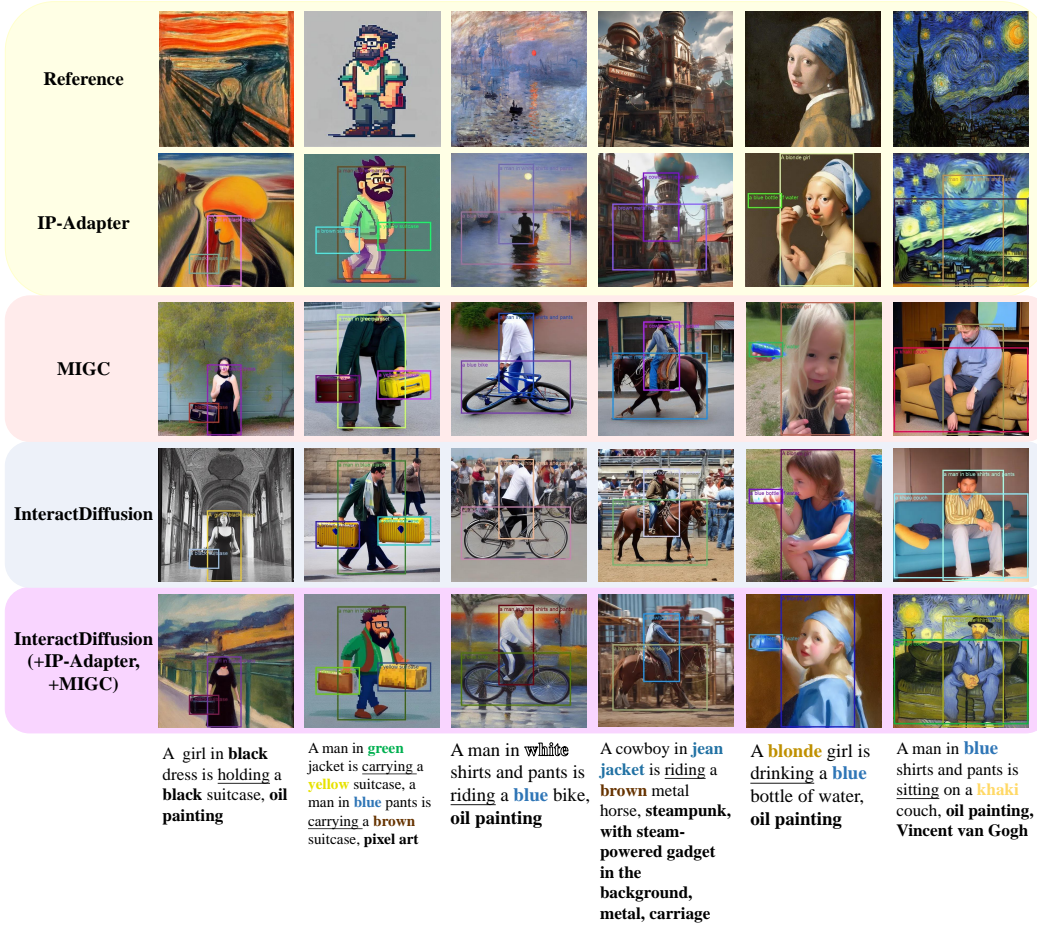


Figure 11: Additional Visual results of aggregating MIGC and IP-Adapter into InteractDiffusion applying the AMDM algorithm.